SIGNAL CONSTELLATIONS OF A RETRODIRECTIVE ARRAY PHASE MODULATOR

A Thesis
Presented to
The Academic Faculty

by

Gregory A. Koo

In Partial Fulfillment
of the Requirements for the Degree
Master of Science in
Electrical and Computer Engineering

School of Electrical and Computer Engineering
Georgia Institute of Technology
May 2011

SIGNAL CONSTELLATIONS OF A RETRODIRECTIVE ARRAY PHASE MODULATOR

Approved by:

Professor Gregory D. Durgin, Advisor
School of Electrical and Computer Engineering
Georgia Institute of Technology

Professor Mary Ann Ingram
School of Electrical and Computer Engineering
Georgia Institute of Technology

Professor Andrew F Peterson
School of Electrical and Computer Engineering
Georgia Institute of Technology

Date Approved: 4 April 2011

To my friends and family

who have showered me with support,

thank you for believing in my dreams and aspirations.

ACKNOWLEDGEMENTS

I would like to thank everyone on my committee for volunteering their time. To Dr. Gregory Durgin, thank you for advising me over the years and answering my many questions. To Dr. Ingram and Dr. Peterson, thank you for serving on my committee and offering your valuable time and resources.

TABLE OF CONTENTS

LIST OF TABLES

LIST OF FIGURES

SUMMARY

A quadrature phase shift keying (QPSK) retrodirective array phase modulator (RAPM) was designed and fabricated to characterize its backscatter signal constellation when placed near objects with varying conductivities and relative permittivities. The signal constellations produced when the RAPM was placed near objects were compared to a constellation in free space to determine relative magnitude and phase changes. When conductors and high permittivity dielectrics were placed close behind the RAPM, constellation points were found to shrink in magnitude by up to twenty percent and shift in phase by up to eight degrees. When conductors were placed between the RAPM and an interrogator, the signal constellation was found to collapse, shrinking by up to 95.6 percent. For materials similar to free space, minimal constellation shrinkage resulted, but signal constellation rotation by up to 68 degrees occurred. The power consumption of a RAPM was also characterized and found to decrease as the number of bits per symbol increased. This result demonstrates that in comparison to conventional backscatter tags, which implement one bit per symbol, the RAPM can implement a greater number of bits per symbol, reduce its power consumption, and increase its range in a passive backscatter communication system. To characterize the beamwidth of the RAPM's retrodirective array, a radar cross section (RCS) measurement of the RAPM was performed over a scan angle range of -90 to +90 degrees. The structural component generated by the RAPM's patch antenna ground plane was found to dominate the antenna mode of the retrodirective array. As a result, a novel homodyne receiver based RCS measurement was performed to filter out the structural RCS component and measure the pure antenna mode of the RAPM.

CHAPTER I

INTRODUCTION

Passive backscatter sensing is a unique field of electromagnetics that involves communicating information without the need for external power from batteries or power grids. In the field of RFID, these backscatter sensors, or "tags", are implemented in areas such as supply chain logistics and anti-theft devices. Such devices have been historically limited in bandwidth and range, due the minuscule amounts of power that can be harvested from incident RF and used to power the ICs onboard the tag, but ongoing research in the area of backscatter devices has advanced the technology and allowed passive tags to operate at distances never seen before. As a result, the increase in distance is now making it difficult to decode the backscattered information, since backscattered power levels at the interrogator are becoming signal to noise ratio limited. To remedy this problem, methods for increasing the amount of backscattered power have recently become of interest, and this thesis presents the retrodirective array phase modulator (RAPM) as a solution for increasing the backscattered signal power and reducing tag power consumption.

1.1 A Backscatter System

The two main elements comprising a full backscatter communication chain are the reader, also called the interrogator, and the tag. The interrogator is the driving source behind link operation. Typical interrogators transmit a continuous wave (CW) signal that powers up a passive tag on the forward link and is backscatter modulated to encode information on the reverse link. Since the tag is inherently power limited, the majority of processing is implemented at the interrogator, which must accurately detect and decode the minuscule backscattered signal. A high level system diagram

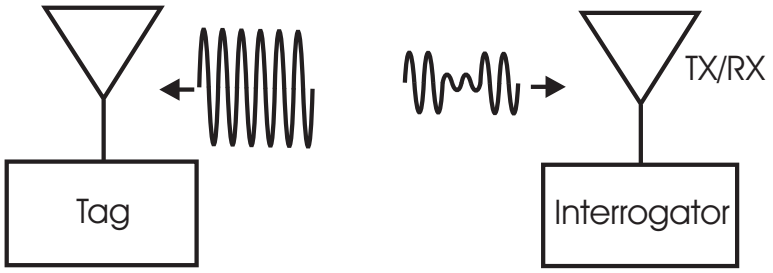

Figure 1: Simplified diagram of a backscatter system. On the left, CW impinges on the tag and is backscatter modulated back toward the interrogator on the right.

demonstrating impinging CW and modulated, backscattered CW is shown in Figure 1.

1.1.1 Backscatter Interrogator

There are three primary antenna configurations available for an interrogator: monostatic, bistatic collocated, and bistatic dislocated, as shown in Figure 2. The monostatic case implements a single antenna at the interrogator and utilizes a circulator or directional coupler to separate the transmit and receive signals. A monostatic implementation requires the smallest form factor and is commonly implemented in handheld readers and security access systems but suffers from large amounts of self-interference due to carrier leakage into the receive chain. Circulators typically provide up to 30 dB of isolation between the transmit and receive chains, but for 1 watt, or 30 dBm, of transmit power, that means 0 dBm of the transmitted carrier leaks back into the receive chain. As a result, this large amount of self-interference dominates the much smaller backscatter signal that is received from a tag, decreasing receiver sensitivity.

For the bistatic configurations, the amount of isolation between the transmit and receive chains increases dramatically due to sufficient electrical spacing between the transmit and receive antennas. For the collocated case, between 40 dB and 50 dB

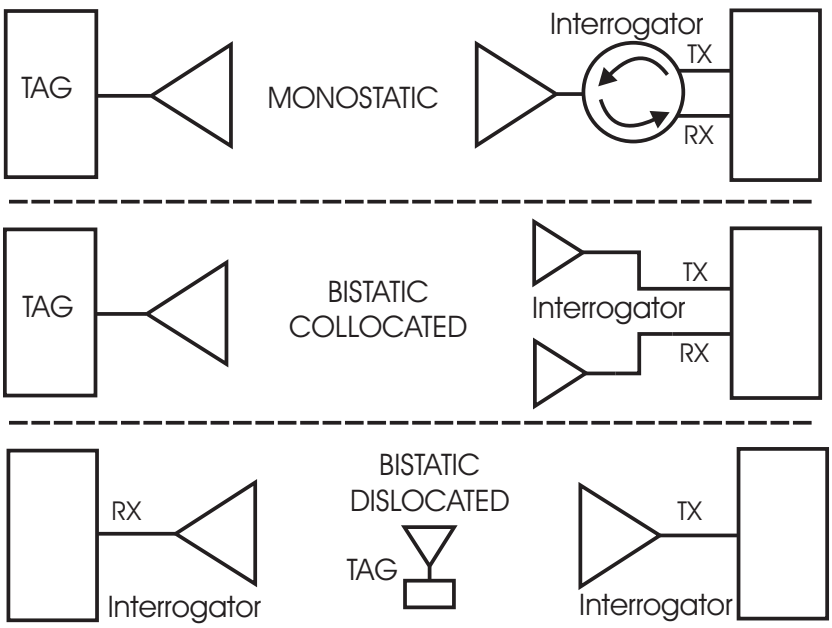

Figure 2: Top: Monostatic configuration. Middle: Bistatic collocated configuration. Bottom: Bistatic dislocated configuration.

of isolation is typically achieved [3]. Improved performance under small signal fading can also be achieved by implementing bistatic configurations, with the dislocated implementation yielding the smallest fade margins [4]. The reason for such increased performance under fading can be attributed to antenna diversity and reduced correlation between propagation paths.

1.1.1.1 Passive Self-Interference Removal

Yet bistatic configurations still suffer from self-interference and additional steps must be taken to remove the unwanted leaky carrier signal. Two different approaches exist, passive carrier suppression and active carrier suppression. In terms of complexity, passive suppression techniques are the simplest to implement, since little to no additional hardware is required. By controlling the physical separation of transmit/receive antennas and employing polarization diversity between the antennas, isolation of up

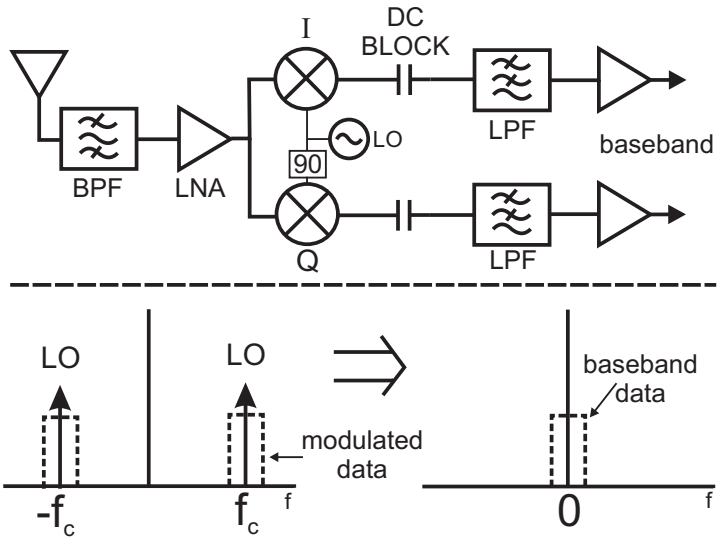

Figure 3: Top: Schematic of direct-conversion receiver. Bottom: Frequency domain operation performed by the receiver.

to 50 dB can be achieved for an RFID receiver [5]. Another passive suppression technique used to remove the self-interference is to use a direct-conversion, or homodyne receiver that mixes the RF signal directly to baseband, as shown in Figure 3. By mixing the received signal with its own carrier, the leaky carrier gets mixed directly down to zero hertz and becomes a DC voltage that can then be removed by a passive element such as a DC block. The modulated backscatter signal then passes through the DC block with minimal attenuation, assuming its main spectral component is sufficiently above the cutoff frequency of the DC block. The simplicity involved with employing a homodyne receiver to remove the self-interference is appealing, but the major downside to this technique is that the RF front-end of the receiver must be have high dynamic range and high sensitivity in order to amplify the small backscattered signal while not being saturated by the strong self-interference. As a result, the RF front-end must be overdesigned to handle this problem.

1.1.1.2 Active Self-Interference Removal

As shown in Figure 4, to remove the self-interference by means of active suppression, a copy of the carrier signal is fed into the receive chain with the correct phase and amplitude necessary to cancel out the carrier signal that leaks from the transmit antenna into the receive antenna or between circulator ports for the monostatic case. The additional hardware required is a phase shifter and variable gain amplifier (VGA), or a device such as a vector modulator, that allows for the phase and magnitude of a signal to be varied. For the direct conversion receiver, the VGA and phase shifter can be adjusted manually to minimize the DC voltage observed after mixing the received signal down to baseband. For a static channel, this manual adjustment of the leaky carrier cancellation circuitry is sufficient to remove the constant component of self-interference that occurs due to direct coupling between the transmit and receive chains, but for a mobile channel, active control of the leaky carrier cancellation circuitry must be employed due to the time varying component of self-interference that is generated by scatters in the environment as well as by the structural mode of RF tag antennas.

To demonstrate the influence that local scatters have on the self-interference power, it has been shown that at 915 MHz, a single manual adjustment of the carrier suppression circuitry provided a minimum improvement in the signal to self-interference ratio (SSIR) of 22 dB as an RF tag was moved within a room. In contrast, when active adjustment of the carrier suppression circuitry was implemented, a minimum SSIR improvement of 43 dB was achieved. The active adjustment therefore achieved 21 dB more of self-interference suppression than the single manual adjustment [1].

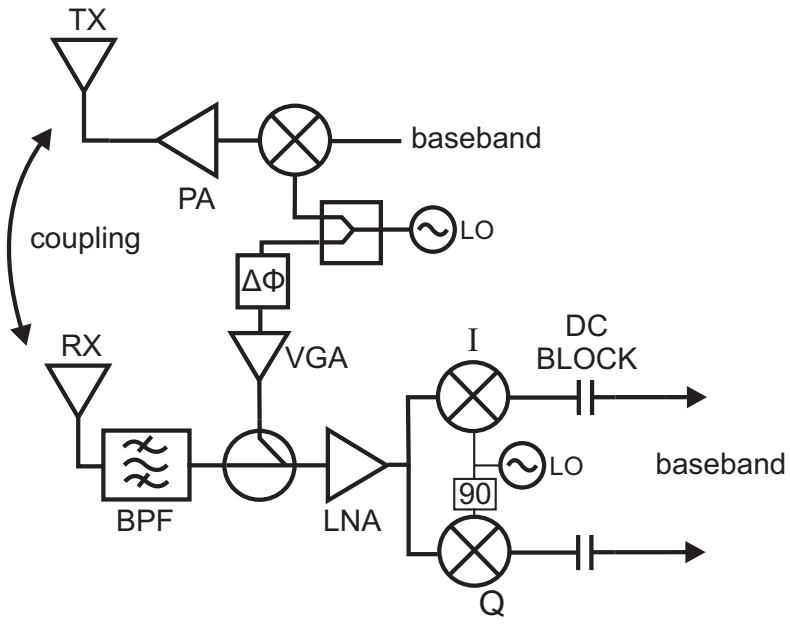

Figure 4: An active suppression bistatic receiver that feeds a copy of the carrier into the receive chain and adjusts the phase and magnitude of the copied signal to cancel out the transmitted carrier that couples into the receive chain [1].

1.1.2 Backscatter Tag

RFID tags are inherently simple devices due to the very low amounts of power that they require to operate. Passive tags implementing the Gen2 RFID standards, found in [6], have been shown to operate at power levels in the range of 1-2 μW, even when the on-board clock rate is 1 MHz [7]. The main reason for such low levels of tag power consumption results from the fact that the power for the tag must be scavenged from ambient electromagnetic energy. As a result, as much processing and hardware as possible has been built into the interrogator in order to facilitate simplistic tags.

1.1.2.1 Backscatter and Load Modulation

To perform communication, passive tags do not require any active RF circuity such as oscillators, mixers, or power amps. Instead, they rely upon the principle of backscatter to perform communication. A classic example of the concept of backscatter can be found in the field of radar, where the tracking of a target is achieved by sending out

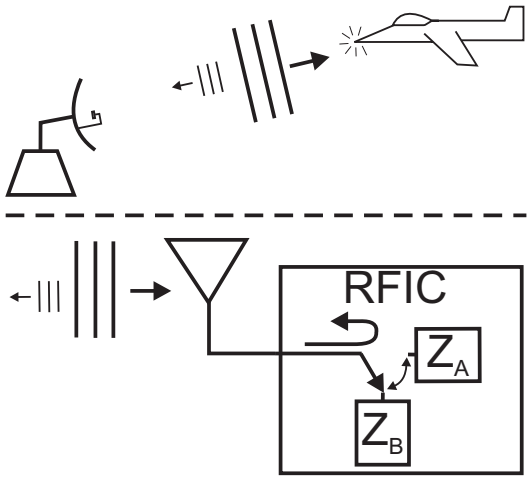

Figure 5: Top: Radar example demonstrating an impinging RF wavefront and its resulting backscattered reflection. Bottom: RFID tag that performs backscatter communication through antenna load modulation.

pulses of electromagnetic energy in specific direction and observing the return pulses, as shown in Figure 5. The fundamental principle that explains why a return pulse is generated can be tied back to the theory of impedance discontinuities. When a wavefront propagates through space and encounters an object with an impedance different to that of free space, a reflection occurs at the impedance boundary and a portion of the incident electromagnetic energy must reflect back toward the source.

A similar principle applies to backscatter communication, which relies upon the antenna mode of the antenna rather than the structural mode. For example, in Figure 5, CW transmissions from an interrogator impinge upon a tag's antenna, travel down the antenna feed, and are partially absorbed or reflected upon encountering a terminating load at the end of the feed. The current flow generated by the voltage excited at the antenna causes the tag's antenna to re-radiate a signal. Typically, two different load states are implemented in the RFIC's that connect to an antenna, with one of the loads being a conjugate match to the antenna in order to maximize power transfer from the antenna into the RFIC, where it is rectified and used to power the chip.

However, due to the nonlinear impedance characteristics of the RFIC, its impedance is highly dependent upon both excitation frequency and input power levels. To overcome this problem and optimize the operational range for a tag, the conjugate match between the antenna and one of the load states is calculated based upon the input impedance of the load when at the very edge of the tag's operating range [8]. By doing so, maximum power transfer occurs when minimum power is available to the tag. Then, as the tag moves closer to the interrogator and its impedance changes, reducing power transfer, the mismatch becomes less significant since greater power is available at the reduced reader-interrogator separation distance.

1.1.2.2 Charge Pumps

The task of powering a passive RFIC is a crucial factor in RFID system operation. Due to path loss and a typically large transmit antenna beamwidth, the power radiated from the antenna at the interrogator decays rapidly as a function of the distance squared, making it critical for the tag to convert as much power as possible from RF to DC. To perform the energy conversion, the most common technique in the field of RFID is to implement charge pumps, specifically the Dickson charge pump. Created in 1975 by John F. Dickson, his charge pump design provided the ability to create the 30V to 40V write voltages required by MNOS nonvolatile memories [9].

To explain the basic operation of a charge pump, a four stage design is provided in Figure 6. On the left is Dickson's conventional design, where the charge pump operates by implementing two anti-phase clocks that work to creating the"pumping" action. For example, the first stage in Dickson's design begins to charge the first capacitor as the clock signal, ϕ, drops in voltage and forward biases the first stage diode, allowing charge to flow from the V_{in} node into the first stage capacitor. Since the voltage at the output of the second stage diode is driven high by the anti-phase clock signal, $\overline{\phi}$, the second stage diode is reversed biased, allowing the first stage to

charge up to the voltage given by Dickson's charge pump output equation, shown in (1).

$$V_{out} = V_{in} - V_D + N\left[\left(\frac{C}{C+C_s}\right)\cdot V_\phi - V_D\right], \tag{1}$$

where we set N, the stage number, equal to one and assume that the parasitic capacitance, C_s, in each stage of the circuit is much less than the capacitance of the stage capacitor, C, allowing us to let $\frac{C}{C+C_s}$=1. The other terms, V_ϕ and V_D, are then replaced with the peak-to-peak magnitude of the clock signal and the forward voltage drop of a diode.

After the first clock cycle, assuming the RC time constant of each stage is small enough, the first stage capacitor reaches a DC voltage of $V_{in} + V_\phi - 2V_D$. During the next clock cycle, the clock signal driving the output of the first stage swings positive and the first stage diode becomes reversed biased while the anti-phase clock signal driving the second stage drops low enough to forward bias the second stage diode. At this point, the full peak-to-peak voltage of the clock signal is placed across second stage diode and capacitor, pumping charge from the first stage capacitor into the second stage capacitor. As this process is repeated, charge is pumped along the diode chain and accumulates in the capacitors of each stage until a DC voltage given by (1) is reached at the output capacitor of the charge pump. Thus the principle mechanism for increasing the output voltage of each stage is that each charged capacitor provides a DC offset to the AC signals driving the charge pump, with the DC offset increasing by $V_\phi - V_D$ for each stage.

For the conventional RF implementation of Dickson's charge pump, the V_{in} and $\overline{\phi}$ terms go to zero since those inputs are grounded, and the last diode and capacitor in the chain are removed, as shown on the right of Figure 6. In Dickson's design, the last diode is only used to prevent clock breakthrough of the signal, $\overline{\phi}$, but in the mono-phase RF implementation, the anti-phase clock signal is removed since the RF carrier wave serves as the only clocking signal. Due to the removal of the anti-phase

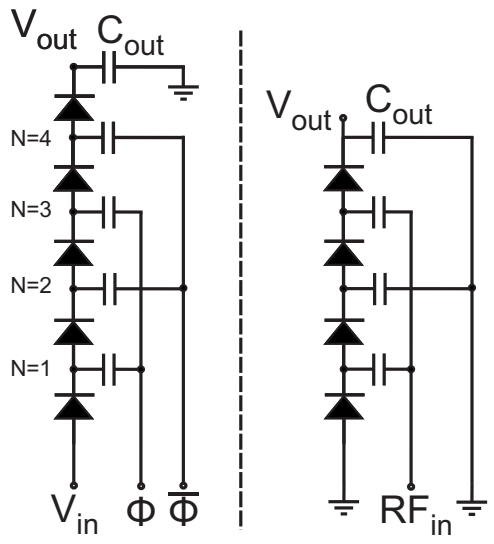

Figure 6: Left: Dickson's original charge pump design that utilizes a bi-phase input, with two anti-phase clocks to perform charging. Right: Dickson charge pump with mono-phase input required for RF operation.

clock, the maximum potential placed across a stage of the charge pump is reduced since the capacitors of the even numbered stages are tied to ground. As a result, the V_ϕ term that was a peak-to-peak voltage reduces by half and is replaced by the magnitude of the $V_{RF_{in}}$ term, resulting in a new charge pump output equation shown in (2). Note that the leading V_{in} term from equation (1) is removed since the V_{in} node is tied to ground for the RF charge pump. The drop from the first diode in the chain is the pushed into the $|V_{RF_{in}}| - V_D$ term, since it still produces a voltage drop during the negative cycle of the RF input signal. The resulting DC output for the RF charge pump then becomes

$$V_{out} = N\left[(\frac{C}{C+C_s}) \cdot |V_{RF_{in}}| - V_D\right]. \tag{2}$$

To demonstrate the operation of the RF charge pump, a four stage charge pump was designed and a transient analysis was performed in LTspice using 1.5 pF capacitors with 0.2 Ω series resistance and Avago HSMS 2862 diodes with an approximate turn-on voltage of 0.3V, as shown in Figure 7. The input to the charge pump was driven by a sine wave source with an amplitude of 1V and a frequency of 5.8 GHz, and

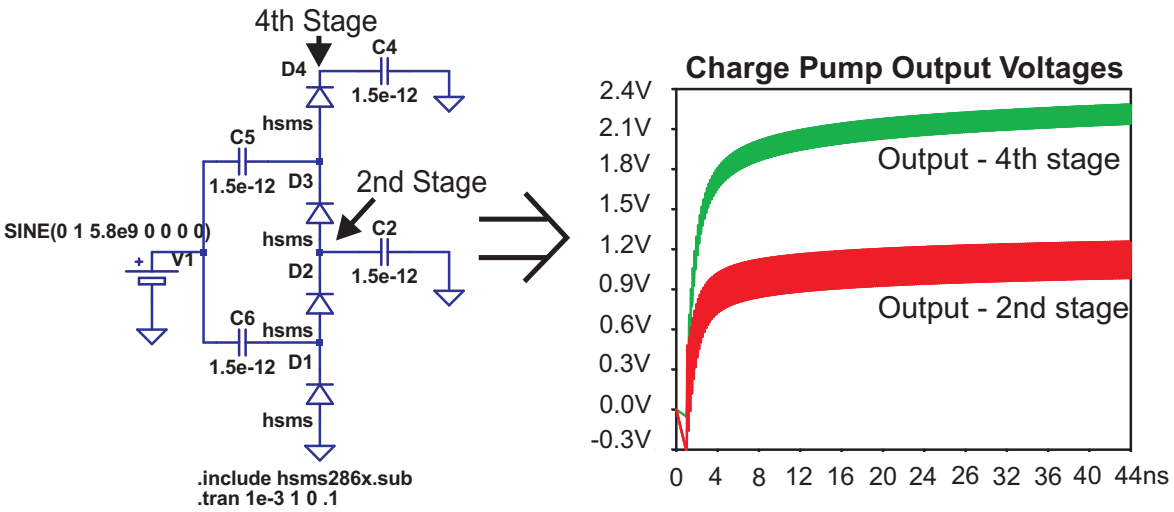

Figure 7: Left: Four stage RF charge pump designed in LTspice, right: Output of 2nd stage and 4th stage under transient analysis.

the output was measured for the second stage and the fourth stage. Note that the duration of the transient analysis of Figure 7 was greatly shortened to demonstrate the fast rise time of the circuit when a small output capacitor is used. The full transient analysis reached a peak steady state voltage of 2.6V at approximately 2 μs, yielding an error of 7.5% in comparison to the 2.8V output predicted by equation (2).

Upon contrasting the RF charge pump with Dickson's original design, an optimization was stumbled upon. By implementing a power splitter at the RF input to the charge pump, an anti-phase clock signal can be created by inserting transmission delays lines that produce phase delays of 180 degrees with respect to the RF input and connecting these delay lines to the even stage capacitors, as shown in Figure 8. To prevent clock breakthrough, the diode and capacitor that were removed from Dickson's design must be replaced, but this new configuration of the RF charge pump allows for a greater potentials to be created across each stage, since the even stage capacitors can now be pulled down to $-V_{RF_{in}}$ instead of a zero volt ground reference. The output voltage of the proposed modified charge pump can then be shown to be

$$V_{out} = -V_D + N\left[\left(\frac{C}{C+C_s}\right)\cdot 0.707V_{RF_{in}} - V_D\right], \tag{3}$$

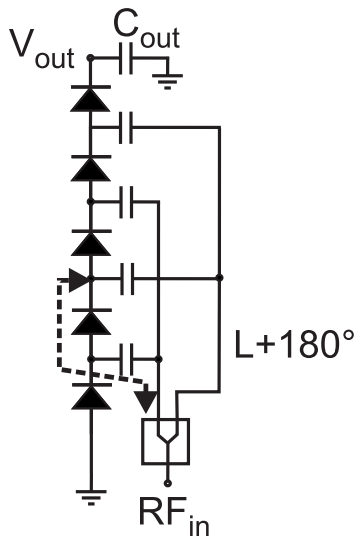

Figure 8: Modified RF charge pump that creates anti-phase clock to increase charge pump output voltage. Dotted line denotes L, the physical length that must be added to the anti-phase feed.

where $V_{RF_{in}}$ is the peak-to-peak voltage rather than the peak voltage. Note that $V_{RF_{in}}$ is the peak-to-peak voltage before the power splitter and its multiplication by 0.707 in equation (3) is results from the Wilkinson power divider, whose the output voltages are 0.707 times in the input voltage. As a result, the proposed charge pump cannot achieve the higher gain of Dickson's charge pump, but instead falls between Dickson's design and the standard RF design in terms of voltage gain.

To validate the proposed charge pump, it was constructed and simulated using LTspice with components identical to the RF charge pump simulation shown in Figure 9. The source voltages were modified from the original 1V amplitude to a 0.707V amplitude to reflect the effects of the Wilkinson power divider. The resulting output at steady state was 3.6V, approximately a 1V improvement over the RF charge pump of Figure 7. Note that charge pump performance can also be improved by using LC resonance techniques between the diode's internal capacitance and the lead inductance of the stage capacitor to produce voltage magnification.

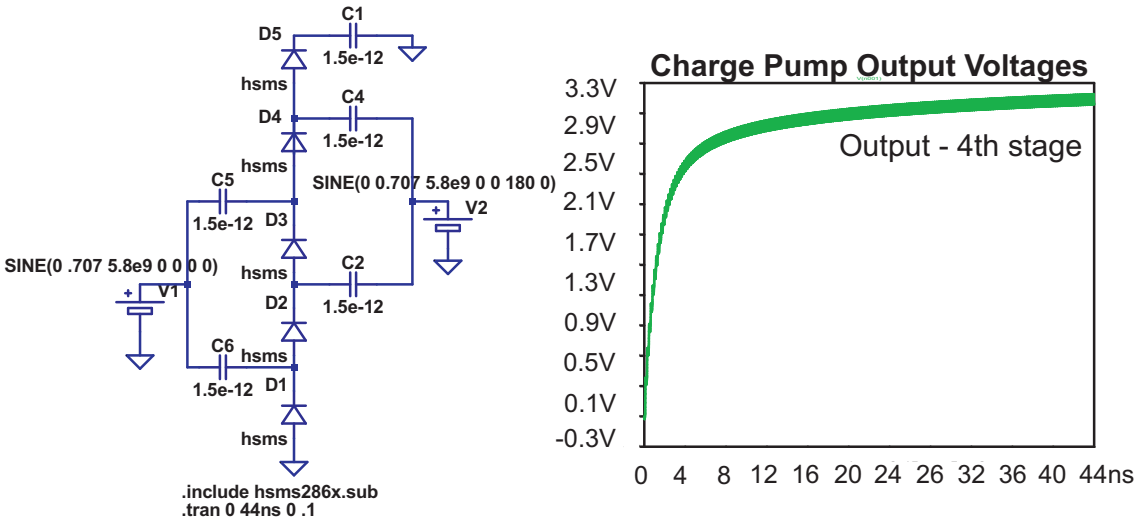

Figure 9: Left: Four stage modified RF charge pump designed in LTspice, right:

1.2 Methods of Communication

The basic mechanism for backscatter communication is the load modulation technique because it allows a single antenna to be used for both powering the RFIC and performing communication. By changing the number of load states available and their respective impedances, modulation techniques such as amplitude shift keying, phase shift keying, quadrature amplitude modulation, and impulse radio ultrawide bandwidth communication can be achieved.

1.2.1 Amplitude Shift Keying

Used as the primary communication method in backscatter systems, amplitude shift keying (ASK), or pulse-amplitude modulation (PAM), is implemented by switching the antenna load of the tag between states with different real components of impedance. In doing so, the amplitude of the signal that is radiated by the tag's antenna is varied, as shown in the signal space and time domain ASK diagrams of Figure 10. To demonstrate the physical processes required for ASK, consider the simplified schematic in Figure 11 that represents an RF tag. The antenna is represented as a source with a resistance defined by the antenna's radiation resistance, R_{rad}. The

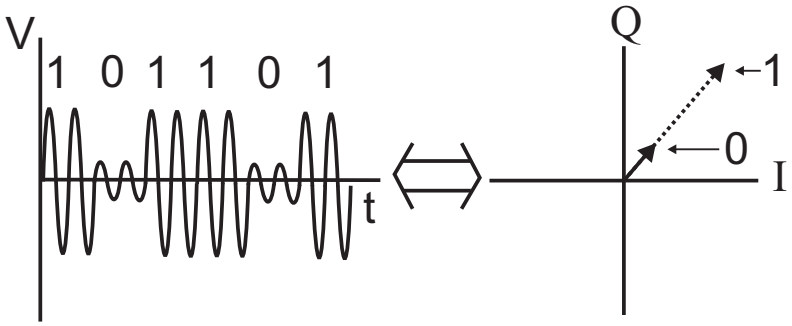

Figure 10: Left: Amplitude modulated 2-ASK backscattered signal in the time domain, right: IQ diagram demonstrating properties of ASK.

amount of power backscattered by the tag can be analyzed using the circuit provided. By solving for the current, i, flowing in the equivalent circuit, the backscattered power can be calculated as follows,

$$P_{backscattered} = i^2 \cdot R_{rad}. \tag{4}$$

The envelope of the backscattered signal is then proportional to $\sqrt{P_{backscattered}}$, which is dependent upon the load resistance. By changing between loads of varying resistance, amplitude modulation can be effectively implemented, and the modulated RF signal can be described as

$$s_m(t) = Re\left[A_m g(t) e^{j2\pi f_c t}\right] = A_m g(t) \cos 2\pi f_c t, \tag{5}$$

where $g(t)$ is a unit pulse whose width corresponds to the symbol rate, and A_m is a discrete amplitude of the backscattered signal that is generated by a specified load resistance.

One specific form of ASK that is worth noting, is on-off keying (OOK), due to its ability to provide the greatest distance between two points in ASK's signal space. In order to perform OOK, the two load states become an open circuit and a short circuit. When the load is connect to the open circuit, no currents flow along the antenna feed, forcing the antenna mode of the backscattered signal to zero and creating the "off" symbol. The structural mode of the antenna will still create some backscatter, but

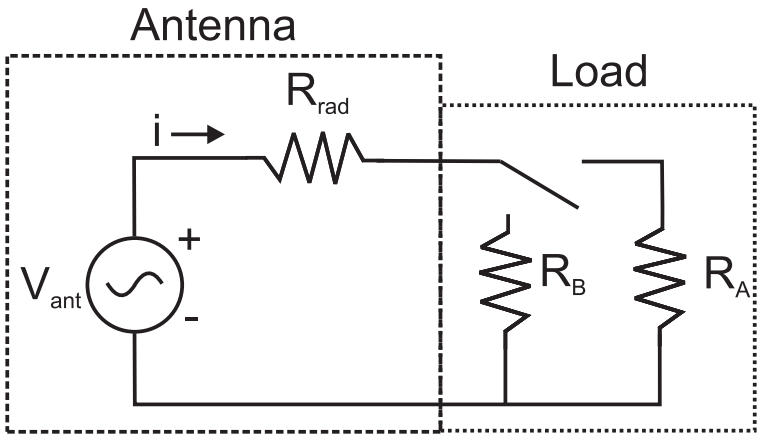

Figure 11: Equivalent circuit representing an antenna with load modulation circuitry.

this typically small component carries no information. To create the "on" symbol, the short circuit load is connected to provide the greatest amount of current flow through the antenna, generating the maximum amount of backscattered energy for a resistive load modulating tag.

1.2.2 Phase Shift Keying

Similar to amplitude shift keying, phase shift keying of a backscattered signal relies upon loads with different reactances to produce phase shifts. The physical phenomenon that allows for phase manipulation stems the from non-linear properties of reactive components such as capacitors and inductors. Since they require time to charge and discharge, the current in a circuit is forced to either lead or lag in phase compared to the voltage, and it is this ability to vary the flow of current that produces a phase shift in the signal radiated from the antenna with respect to the impinging wavefront. For digital phase modulation, the backscattered signal can be defined as

$$\begin{aligned} s_m(t) &= Re\left[e^{j2\pi(m-1)/M} e^{j2f_c t}\right] \\ &= \cos\frac{2\pi}{M}(m-1)\cos 2\pi f_c t - \sin\frac{2\pi}{M}(m-1)\sin 2\pi f_c t, \end{aligned} \tag{6}$$

where the $e^{j2\pi(m-1)/M}$ term denotes the phase shift induced by load m out of M total states and t is defined over a symbol period, T. Here we can clearly see the

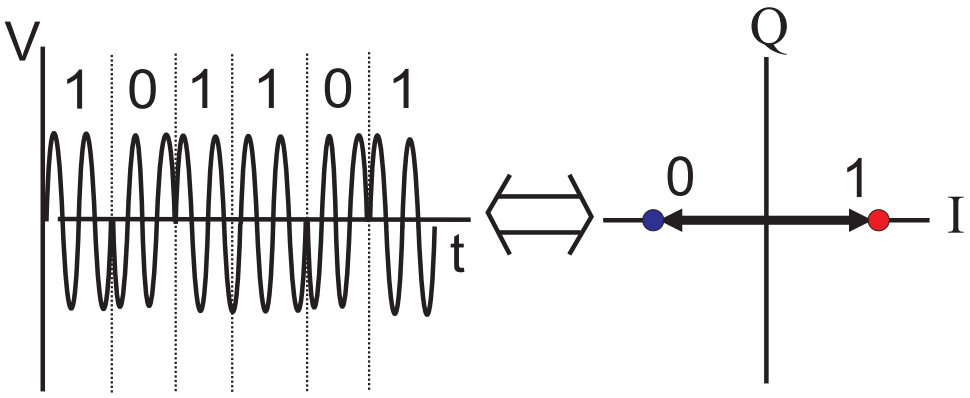

Figure 12: Left: Phase modulated backscattered signal in the time domain, Right: IQ diagram of an ideal BPSK signal.

phase modulation of the carrier term and its respective in-phase and quadrature components.

It is worthwhile to discuss one of the most common forms of PSK, binary phase shift keying (BPSK). To perform BPSK, the loads must be capacitive and inductive in order to produce phase shifts of 90 and -90 degrees in the antenna current. An example of a BPSK backscattered signal is shown in Figure 12 to demonstrate a BPSK signal in the time domain and signal space.

1.2.3 Quadrature Amplitude Modulation

By making the load impedances complex, both the amplitude and phase of the backscattered signal can be manipulated to provide quadrature amplitude modulation, or QAM. The ability to control both the phase and amplitude of the backscattered signal allows for more efficient use of signal space, since the signal vector can be placed anywhere in the two dimensional space. The backscattered signal over a symbol period can be shown as

$$\begin{aligned} s_m(t) &= Re\left[(A_{mc} + jAmse^{j2f_c t}\right] \\ &= A_{mc}\cos 2\pi f_c t - A_{ms}\sin 2\pi f_c t, \end{aligned} \tag{7}$$

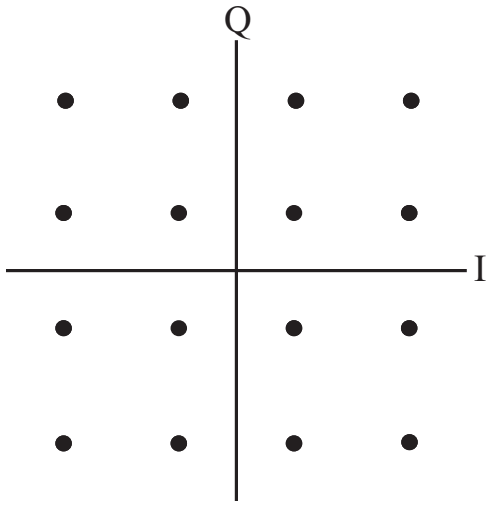

Figure 13: Signal constellation for rectangular 16-QAM

where A_{mc} denotes the change in backscattered signal amplitude produced by the resistive component of load state m's complex impedance, and A_{ms} represents the change in backscattered signal phase produced by the reactive component of load state m. In contrast to QAM, PSK only allows rotation of a constant magnitude signal vector about the origin of the complex plane, and ASK only allows constellation points to be mapped to a one dimensional space. To demonstrate this signal space benefit of QAM, a 16-QAM signal constellation is provided in Figure 13. For a more detailed analysis of design and performance of QAM backscatter devices, see Thomas' article in [10].

1.2.4 Impulse Radio Ultrawide Bandwidth

Relying upon the principle of load modulation, impulse radio ultrawide bandwidth (IR-UWB) communication requires little to no change of existing backscatter tag designs. The major difference from the aforementioned communication schemes is the type of signal transmitted by the interrogator. In contrast to a continuous wave signal that is transmitted at a specific carrier frequency, IR-UWB does not require an RF carrier and instead uses nanosecond pulses that are created at baseband. The

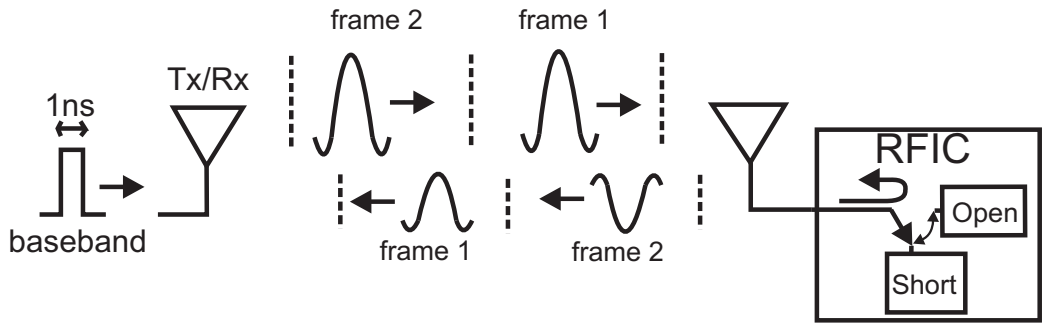

Figure 14: Backscatter system implementing IR-UWB transmission scheme.

ultrashort pulses create a very wide spectral mask that spreads the signal energy over a spectrum that stretches from 3.1GHz up to 10.6 GHz, with the requirement that the maximal power spectral density be less than or equal to -41.3 dBm/MHz [11].

For implementing backscatter communication, a backscatter tag is typically synchronized with the interrogator so that it changes modulation states at the end of each transmission frame, as shown in the antipodal UWB system of Figure 14. The synchronization between a tag's state change and the system frame rate is required to allow for multipath and clutter rejection when a spread spectrum sequence is used to control the load state of a backscatter tag. It also ensures that the tag does not switch states during the time that a pulse is reflecting from the load. To do so would destroy the pulse shape and inhibit the interrogator's ability to detect the pulse's polarity.

As an example of UWB backscatter operation, we will consider a BPSK implementation where a tag implementing a pseudo random sequence will change its modulation state at the end of each frame with respect to each bit of the spreading sequence. The physical result is that for each pulse transmitted by the interrogator, a reflected pulse is generated by the tag with either a positive or negative polarity. After a complete cycle of the spreading sequence is modulated, the interrogator can then detect the tag's response by performing matched filtering on the received pulse train. By combining nanosecond pulses in a de-spreading operation, the effects of multipath are

mitigated while allowing for multi-user access and object ranging. To demonstrate the communication ability of IR-UWB in backscatter systems, Dardari et al. demonstrated that operational distances greater than 20m can be achieved for bitrates of 1kbps [12].

For communication and ranging, IR-UWB demonstrates capability, but for fully passive backscatter systems, the lack of a CW signal makes powering up the tag more difficult since the amount of energy transmitted under a IR-UWB communication scheme is strongly tied to the data rate of the application, which sets the pulse rate of the interrogator. For a passive application, either an additional transmitter generating CW or an increased pulse rate could be used to remedy the problem of powering passive tags. For the increased pulse rate method though, care must be taken to ensure that the rate of charge accumulation in the supply capacitor of the charge pump exceeds the RC discharge rate created by the output capacitor and the load of the RFIC's digital logic.

1.3 Backscatter Channel

Relying upon reflected power rather than a transmitted signal, the backscatter channel is inherently more lossy than the traditional one-way channel. The most profound difference between the two channels can be seen through the free space transmission formula. Derived in 1946 by Harald T. Friis, his equation, shown below, has provided a simplistic method for calculating the amount of power received for a one-way channel [13].

$$\frac{P_r}{P_t} = \frac{A_r A_t}{d^2 \lambda^2}, \tag{8}$$

where d is the distance between the transmit and receive antennas, λ is the free space wavelength, P_r is the power received at the receive antenna, P_t is the power fed into the transmit antenna, and A_r and A_t are the effective areas of the receive and transmit antennas. Note that Friis derived his transmission formula under the

assumption of plane wave propagation. This requires that the distance between the transmit and receive antennas be great enough to place system operation in the far-field or Fraunhofer region. To meet this requirement, Friis states the separation distance, d, as

$$d \geq \frac{2a^2}{\lambda}, \tag{9}$$

where a denotes the largest linear dimension of either the transmit or receive antenna.

1.3.1 Link Budgets

Friis' original notation focuses upon the power transmitted, the frequency of operation, and the effective apertures of the transmit and receive antennas. While his derivation provides an equation that is conceptually easy to grasp, the parameter of effective aperture is not typically provided in antenna specifications today. More modern versions of the Friis formula replace the effective aperture terms with the more common antenna gain terms. In order to make this substitution, the following relation is applied,

$$A_e = G(\frac{\lambda^2}{4\pi}), \tag{10}$$

where G is the antenna gain with respect to an isotropic antenna.

Griffin et al. proposed specific Friis transmission formulas for the forward power-up backscatter link, the monostatic backscatter link, the bistatic, collocated backscatter link and the bistatic, dislocated backscatter link. The respective linear link equations can be found in [14], and have been listed below.

$$\text{Power-Up Link Budget} \qquad P_t = \frac{P_{Tx} G_{Tx} G_{tag} \lambda^2 X \tau}{(4\pi r)^2 \Theta B F} \tag{11}$$

$$\text{Monostatic Link Budget} \qquad P_R = \frac{P_{Tx} G_{Tx/Rx}^2 G_{tag}^2 \lambda^4 X^2 M}{(4\pi r)^4 \Theta^2 B^2 F_2} \tag{12}$$

$$\text{Bistatic, Collocated Link Budget} \qquad P_R = \frac{P_{Tx} G_{Tx} G_{Rx} G_{tag}^2 \lambda^4 X^2 M}{(4\pi r)^4 \Theta^2 B^2 F_\alpha} \tag{13}$$

$$\text{Bistatic, Dislocated Link Budget} \qquad P_R = \frac{P_{Tx} G_{Tx} G_{Rx} G_{tag}^2 \lambda^4 X_f X_b M}{(4\pi)^4 r_f^2 r_b^2 \Theta^2 B_f B_b F_\beta}, \tag{14}$$

The power-up link budget, shown in equation (11) describes the amount of power available at the input of a backscatter tag's charge pump, where r is the separation distance between an interrogator and tag, P_{Tx} is the power transmitted by an interrogator (W), G_{Tx} is the gain of the transmit antenna, G_{tag} is the gain of the backscatter tag's antenna, and λ is the free-space carrier wavelength. The remaining terms, X, τ, Θ, B, and F are unitless factors added to the original Friis equation to account for losses incurred through polarization mismatch, charge pump conversion efficiency, on-object gain penalties, channel blockage loss, and fading, respectively.

Comparing the power-up budget, which is essentially a one-way link, to the monostatic backscatter link budget, it becomes clear that the multiplicative nature of the backscatter channel greatly increases the channel loss. This increase in loss can be attributed to squaring the $\frac{\lambda}{4\pi r}^2$, X, Θ, and B terms, with the greatest increase in loss resulting from the free space path loss term, $\lambda/4\pi r$, due to the inverse-square law increasing from the second power to the fourth power. To demonstrate the increase in path loss between a one-way link and a backscatter link, Figure 15 plots the received power for a 5.8 GHz system with isotropic antennas, 30 dBm transmit power, and free space path loss. Note that 30 dBm was selected since it is the maximum transmit power allowed for the 5.8 GHz ISM band. As we can see at 1m, the backscatter

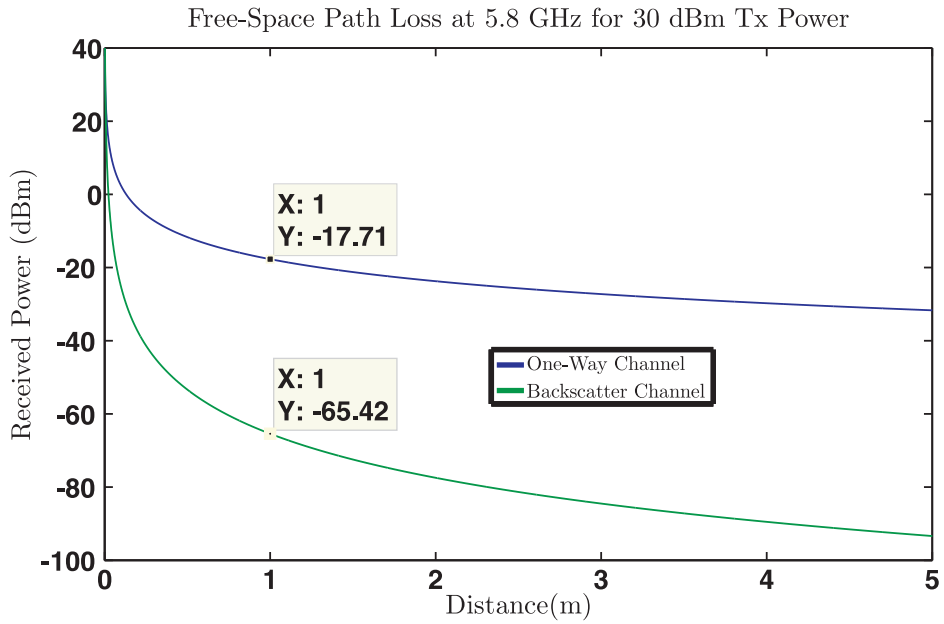

Figure 15: Backscatter system implementing IR-UWB transmission scheme.

channel loss is 47.7 dB more than the one-way link. The monostatic backscatter link, however, accounts for a total signal travel distance of $2r$, since the signal propagates from the interrogator to the tag and back, so a more realistic comparison between the one-way link and monostatic link would be to find the path loss of a one-way link at 2m. In this case, we look at the Figure 15 and see that for the one-way link at 2m, we receive -23.3 dB. In comparison to the monostatic backscatter link at 1m, the channel loss for the backscatter link is still 42dB more. For a more detailed explanation of backscatter link budgets, see [14].

1.3.2 On-Object Gain Penalties

The on-object gain penalty term also requires additional attention, since it partially inspired this work. Griffin et al. shown in [15] that for 915 MHz dipoles, the radiation properties were altered when liquid and solid objects of varying relative permittivity and loss tangents were placed in a dipole's immediate half-space. For materials such as cardboard, with $\epsilon_r \approx 1$, the dipole's gain decreased by only 0.9dB on average, but

for materials such as ethylene glycol, with a higher permittivity of $\epsilon_r \approx 7.6$, average gain penalties of 7.6dB were measured.

The fundamental reason for the antenna gain reduction is that the near field power generated by the antenna couples into surrounding materials with permittivities higher than air, robbing power from the desired direction of radiation [15]. Since environmental conditions have been shown to influence the gain pattern of the dipole so greatly, it is expected that even for antennas with ground planes, such as the patch antenna, radiated signals and their resulting signal constellation patterns will also be affected.

1.4 Retrodirective Array

Developed in 1955 by L.C. Van Atta, the retrodirective array (RA) holds the unique property that any impinging waveform is reradiated back toward the source [16]. Unlike smart antennas that use active beamsteering, Van Atta's design does not require additional hardware such as phase shifters or local oscillators but instead relies upon antenna symmetry and special restrictions on feed lengths.

1.4.1 Theory of Operation

To provide an understanding of how retrodirectivity occurs, a brief analysis showing the interaction between a RA and an incident wavefront is presented. Figure 16 shows a basic four element, linear, equally-spaced RA constructed with identical antennas that are mirrored with respect to the centroid, or inversion point of symmetry, of the array. Beginning with the inner antenna pair, an arbitrary length transmission line is connected between the two radiating elements. Each additional antenna pair must then be connected by a transmission line of length d or $d + n\lambda$, where n is a positive, real integer. This constraint arises from the need to maintain the relative phase offset that occurs between each antenna when an oblique wavefront impinges upon the array. Without these electrically identical lengths, undesired destructive interference

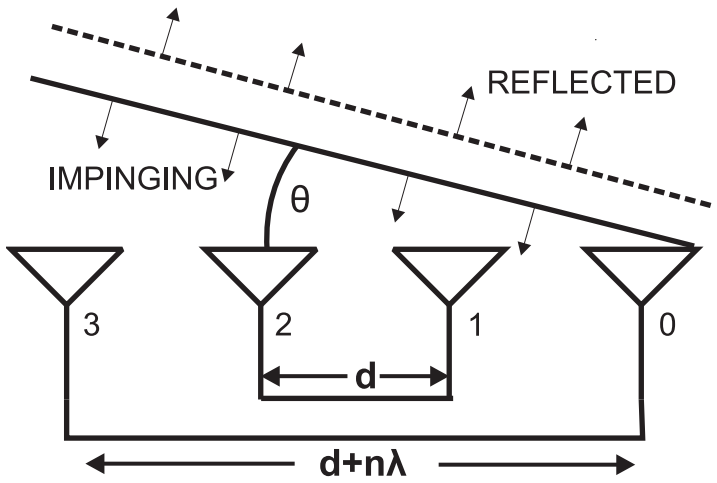

Figure 16: 4-Element retrodirective array with incident and reradiated wavefronts.

occurs in the wave reradiated back toward the source and retrodirectivity is no longer achieved. Shown at the top of Figure 16, an impinging wave encounters the zeroth antenna element. The phase difference of the wavefront at each antenna, with respect to the zeroth antenna element, can be shown in radians as

$$\phi_{diff} = \frac{2\pi \cdot \sin(\theta) \cdot a \cdot d}{\lambda_0}, \tag{15}$$

where θ is the angle of incidence with respect to broadside, a is the antenna index of the array, and d is the physical spacing between antenna elements, as shown in Figure 16. As the antennas on the right side of the array absorb the impinging wave, relative phase differences are maintained as the waves propagate down the lines connecting each antenna pair. These traveling waves are then reradiated by the antennas on the left side of the array's inversion center. The same process occurs after the incident wave reaches the antennas to the left of the inversion center of the array. In the case of Figure 16, the wave is absorbed by antennas 0 and 1 and reradiated by antennas 3 and 2, respectively. Antennas 2 and 3 then absorb the wavefront at a later point in time, and antennas 1 and 0 reradiate the wave. After this complete cycle, a uniform wavefront propagates back toward the radiating source.

CHAPTER II

RETRODIRECTIVE ARRAY PHASE MODULATOR

Built upon Van Atta's design, the retrodirective array phase modulator (RAPM), uses L antenna elements to provide an L^2 increase in linear backscattered power when compared to a single antenna. By harnessing the passive phase combining properties of a retrodirective array, the RAPM's reradiated signal arrives in phase at the interrogator and provides a maximal Signal-to-Noise Ratio (SNR). The RAPM also has the ability to perform higher order PSK, which decreases the symbol rate necessary to achieve a given bit rate. As a result, the operational duty cycle for the baseband circuitry onboard the tag that drives the communication of the retrodirective array can be decreased, lowering on-tag power requirements and allowing greater operational range. Smith et al. demonstrated that for the WISP architecture, which utilizes a microcontroller as the tag's baseband processor, the read range of an RF tag more than doubled when the microcontroller duty cycle was decreased to 1/9 th [17]. Using a retrodirective array in a backscatter system thus provides tremendous benefit for backscatter radio operation, where read range depends strongly upon tag power consumption and backscattered power levels.

2.1 Alternatives to a RAPM

Before creating the RAPM design, a thorough literature review was performed to determine competing designs that implement arrays on the backscatter link. A survey of such devices is provided below to help distinguish the properties of the proposed RAPM, especially for passive backscatter systems.

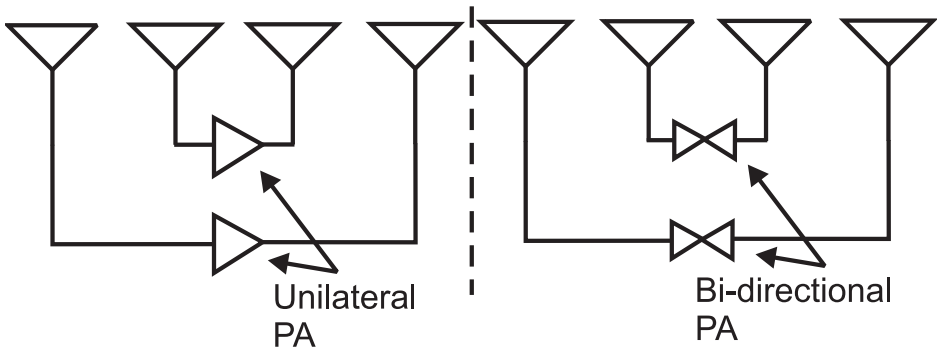

Figure 17: Left: Retrodirective array with inline unilateral power amplifiers. Right: Retrodirective array with bi-directional power amplifiers

2.1.1 Power Amplifier Technique

One implementation of a retrodirective array uses amplifiers placed in series with the antenna pair feeds, as shown in Figure 17. By placing either unilateral or bi-directional amplifiers in series, the amount of backscattered power can be greatly increased, extending the read range of systems that are power limited on the reverse link, as shown by Chung et al., who achieved a peak power gain in the reradiated signal of 9.1 dB [18]. Using the power amplifier technique, OOK communication can also easily be performed by turning the PAs on and off, but for passive systems, the PA technique requires too much power for amplifier biasing and cannot be supported solely by RF energy scavenging over usable distances or transmit power levels.

2.1.2 Pon Array

Proposed by C.Y. Pon in 1964, the Pon array, or heterodyne array, utilizes a common LO source, a mixer, and a circulator at each antenna element to produce the conjugate phase shift required to reradiate a signal back toward the source, as shown in Figure 18. By using the heterodyne technique to mix the received signals with an LO of twice the carrier frequency of the received signal, the lower sidebands that result after the mixing process have the same frequency as the received signals but conjugate phases [19]. This mimics the passive phase conjugation that occurs in a

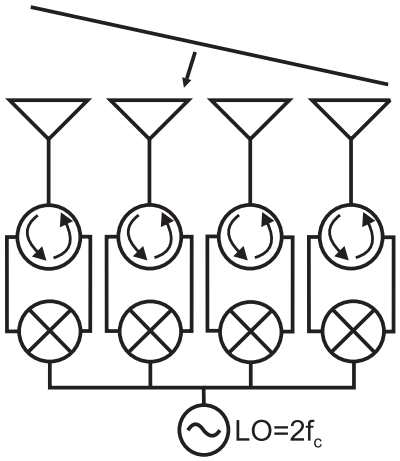

Figure 18: Four element Pon array with an LO at twice the carrier frequency of the received signal.

traditional retrodirective array. The conjugated signals are then fed back into circulators and reradiated to generate an equiphase wavefront that propagates back toward the source.

To perform ASK on the reradiated signals, the LO drive power into the mixer can be adjusted to increase or decrease the mixer's conversion loss, which thereby varies the magnitude of the reradiated signal. The Pon array can also be made into a full duplex system with a slight design change. To perform both up and downconversion, two series mixers are used instead of one, and they are driven by an LO that mixes down to an IF frequency. After the first mixing stage, the received signal becomes IF and can be demodulated to recover data transmitted by the interrogator and then mixed back up to RF and transmitted with the required conjugate phase shift [20].

2.1.3 Frequency Steerable Arrays

While not a retrodirective array, the concept of using a parasitic array with different resonant frequencies is an interesting method for increasing the antenna gain and the backscattered power in a given direction. By designing the dimensions of parasitic elements correctly, only certain elements will resonate at a specific frequency, causing

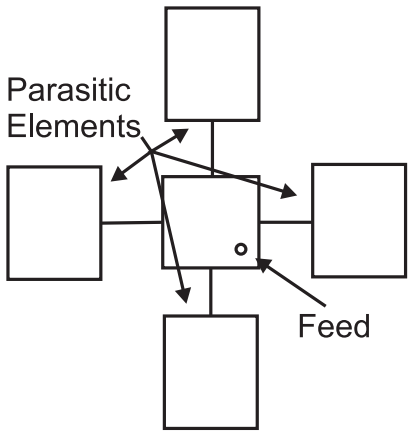

Figure 19: Frequency steerable multi-mode parasitic patch array.

the array's radiation pattern to change. For example, the array shown in Figure 19 is a frequency selective backscatter patch array that was proposed in [21]. It resonates at 5.65 GHz, 5.81 GHz, and 6.2 GHz, with antenna patterns that split the main lobe vertically, horizontally, or focus it broadside. Frequency steerable arrays are also able to implement backscatter communication by applying standard load modulation techniques to the central element's feed, but the true merit to this technique resides in the fact that no additional circuitry or components such as mixers or switches are needed to increase backscattered power.

2.2 RAPM Operation

The novel aspect of the RAPM is that it has the ability to change the phase of a reradiated wavefront. By connecting different lengths of transmission line between antenna pairs, as shown in the QPSK RAPM of Figure 20, specific phase shifts can be induced in the reradiated wave to perform M-ary PSK. The transmission line segments can be individually connected in series with the antenna feeds by controlling a pair of multiple port RF switches via a microcontroller. To construct a multi-antenna RAPM, each antenna pair requires its own set of switches and transmission lines, but only one microcontroller is needed, since the FET switches for all antenna pairs

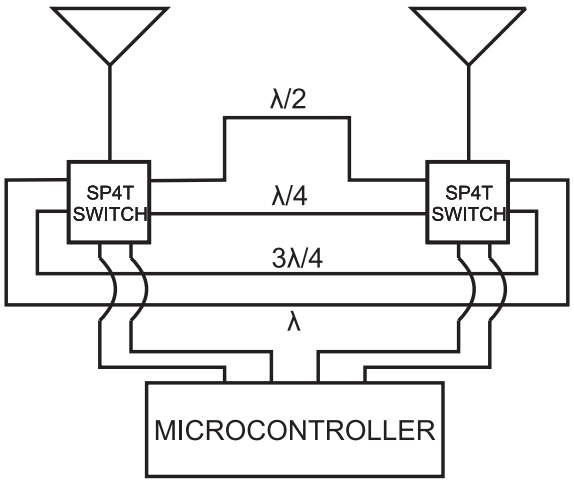

Figure 20: Schematic of a two element retrodirective array phase modulator; Microcontroller simultaneously controls switches that change the phase length of the transmission line connecting an antenna pair.

receive the same control signals.

2.3 Backscatter Signaling Matrix

To characterize the communication properties of the RAPM, a general backscatter signaling matrix, shown in Equation 16, was derived from two-port scattering theory for a lossless, reciprocal RAPM.

$$\bar{S}(t) = \begin{bmatrix} 0 & P & 0 & 0 & \cdots \\ P & 0 & 0 & 0 & \\ 0 & 0 & 0 & P & \\ 0 & 0 & P & 0 & \\ \vdots & & & & \ddots \end{bmatrix}, P = e^{-j\frac{2\pi}{\lambda}\ell(t)} \tag{16}$$

Inside the signaling matrix is the phase shift term, P, which is a function of ℓ(t), the electrical length of the transmission line between the RF switches of an antenna pair. For the specific QPSK scenario, ℓ(t) can be $\lambda/4$, $\lambda/2$, $3\lambda/4$, or λ, resulting in a signal constellation with 90° phase differences between states. Each antenna pair is assigned port numbers, with the innermost antenna pair being ports 1 and 2, the next

innermost antenna pair becoming ports 3 and 4, and so on, as shown in Figure 21, where the innermost antenna pair is labeled with port numbers 1 and 2 to correspond to their respective phase shift terms at indices 1,2 and 2,1 in signaling matrix $\bar{S}(t)$. Note that since the antenna feed network is reciprocal, $\bar{S}(t)=\bar{S}(t)^T$, it is arbitrary to select which antenna corresponds to port 1 or port 2. Thus the phase terms in the signaling matrix at indices 1,2 and 2,1 characterize the phase shift that occurs as the absorbed wave propagates along the feed of the innermost antenna pair. This general $L \times L$ signaling matrix applies to any two or three dimensional retrodirective array with L antenna elements.

2.4 Backscatter Channel Properties

RAPM properties can be further explained through application of the general $M \times L \times N$ dyadic backscatter baseband channel model, where M, L, and N represent the number of antennas at the transmitter, RAPM, and receiver. The general model can be simplified to the monostatic $1 \times L \times 1$ scenario in order to demonstrate the benefits of a retrodirective backscatter device. For a more detailed analysis of dyadic backscatter channels, see references [22] and [23]. For the forward channel, the path from the interrogator to each array element is assigned a unique channel coefficient since diversity branches arise from spatial separation of the antennas. For the backward channel coefficients, they are identical to the forward coefficients since forward and backward propagation paths in the monostatic case are assumed to be fully correlated, with ρ=1. A full characterization of the backscatter channel can then be achieved by combining the forward channel coefficients, the backward channel coefficients, and the signaling matrix of the RAPM as shown in equation (17).

We begin by observing what happens to the transmission of a signal, $\tilde{x}(t)$, through a baseband equivalent channel involving a RAPM. This process can be fully described

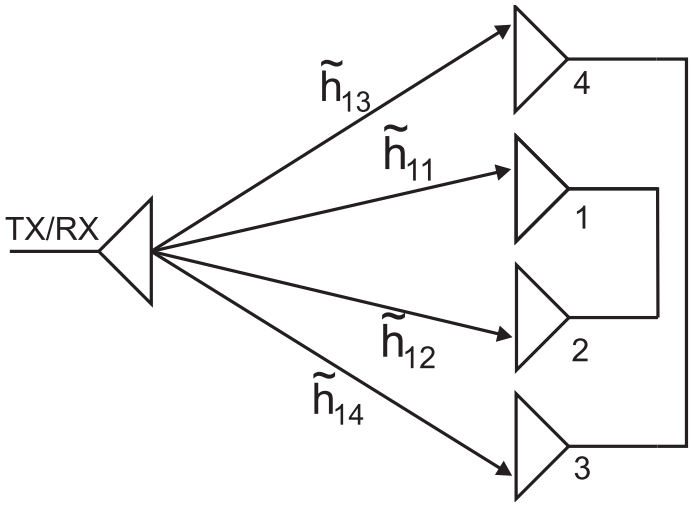

Figure 21: Forward channel for 4 element RAPM using baseband channel coefficients. The backward channel is identical to the forward channel under monostatic conditions.

by the following equation,

$$\tilde{y}(t) = \frac{1}{2}\tilde{\vec{h}}^{b}(\vec{r})\bar{S}(t)\tilde{\vec{h}}^{f}(\vec{r})\tilde{x}(t) + \tilde{n}(t), \tag{17}$$

where the physical channel convention is taken in order to relate the channel coefficients to the voltage measured at the receive antenna's terminals. Also note that $\tilde{x}(t)$ can be simplified to $\tilde{x}$ if the source is an unmodulated RF carrier wave, and that $\tilde{\vec{h}}^{b}(\vec{r})$ and $\tilde{\vec{h}}^{f}(\vec{r})$ are vectors of dimension L.

To create the channel coefficient vectors, the local area approximation is invoked and the general form of $\tilde{\vec{h}}^{f}(\vec{r})$ becomes

$$\tilde{\vec{h}}^{f}(\vec{r}) = \tilde{h}_0 \begin{bmatrix} e^{-j\frac{2\pi}{\lambda_0}\hat{k}\cdot\vec{r}_1} \\ e^{-j\frac{2\pi}{\lambda_0}\hat{k}\cdot\vec{r}_2} \\ \vdots \\ e^{-j\frac{2\pi}{\lambda_0}\hat{k}\cdot\vec{r}_L} \end{bmatrix}, \tag{18}$$

where $\tilde{h}_0$ represents the baseband-equivalent channel response, and the $e^{-jk_0\hat{k}\cdot\vec{r}}$ terms represent phase differences at each RAPM antenna with respect to the RAPM's inversion point of symmetry, assuming that the incident wave is a plane wave. The

distance vectors, $\vec{r}$, whose subscripts correspond to the port numbers assigned during the creation the signaling matrix, are simply vectors from the inversion point of symmetry to each antenna. From equation 18, one can create the $\tilde{\vec{h}}^b(\vec{r})$ row vector by taking the transpose of the forward channel coefficient vector, $\tilde{\vec{h}}^f(\vec{r})$.

The following simplifications can then be applied to Equation 17 to demonstrate the L^2 backscatter power gain produced by the RAPM. We begin by letting the noise component go to zero and letting $\tilde{x}(t)$ be of constant amplitude and unity magnitude. Then,

$$\bar{S}(t)\tilde{\vec{h}}^f(\vec{r}) = \tilde{\vec{h}}^f(\vec{r})^*, \tag{19}$$

since the distance vectors for each antenna pair are equal and opposite. For example, in Figure 21, the distance vectors, with respect to the inversion point of symmetry for the RAPM's array, are $\vec{r}_1$=-$\vec{r}_2$ and $\vec{r}_3$=-$\vec{r}_4$. Since the channel is monostatic and the forward and backward diversity branches are identical, the following relationship then results:

$$\tilde{\vec{h}}^f(\vec{r}) = \tilde{\vec{h}}^b(\vec{f})^t. \tag{20}$$

Applying the relations from equations (19) and (20) to equation (21) then allows us to get $\tilde{y}(t)$ solely in terms of $\tilde{\vec{h}}^b(\vec{f})$, as shown in equation (21). This final version of a received, baseband backscattered signal simplifies to become the L1-Norm of the channel vector, which due to the aforementioned normalization, shows $\tilde{y}(t)$, the voltage measured at the interrogator's receive antenna, to be proportional to L, the number of RAPM antenna elements.

$$\tilde{y}(t) = \tilde{\vec{h}}^b(\vec{r})\tilde{\vec{h}}^b(\vec{r})^\dagger = L \tag{21}$$

This result demonstrates that for a RAPM device operating in a backscatter channel, the channel gain provided through retrodirectivity is a direct function of the number of RAPM antennas. The physical meaning behind equation (21) is that the signals reradiated by each RAPM antenna combine in phase at the transmitter to

produce a maximal SNR. This passive phase combining that takes place at the receiver is analogous to the maximal ratio combining implemented with array processing. The received voltage and power are therefore proportional to L and L^2, respectively.

CHAPTER III

RAPM DESIGN

The main components comprising a RAPM are the antennas and the phase switching network. A prototype QPSK RAPM, shown in Figure 22, was designed and fabricated on FR-4 to allow characterization of its backscatter properties. The design process and its associated hurdles are provided to serve as a design reference and explain the physical characteristics of the RAPM itself.

3.1 Antennas

Half wavelength patch antennas were chosen for the RAPM due to their planar design, moderate beamwidth, and moderate gain. Since RF sensors are typically attached to objects, maintaining a planar design was a driving factor in choosing the antenna topology. As for the beamwidth requirements, a trade-off between directivity and beamwidth was chosen in order to increase the operational range of the RAPM while still maintaining omni-directional characteristics. For a true passive sensing operation however, a more isotropic antenna such as a dipole would be ideal in order to allow for operation under conditions where the orientation of the tag is unknown. In contrast, if the orientation and position of a sensor are known and static with time, high gain antennas such as the Yagi-Uda design or single-port static arrays can be implemented to increase operational range.

3.1.1 Initial Design

The initial width, W, and length, L, for the patch antennas were based upon the following equations that include fringing effects [24]:

$$W = \frac{v_0}{2f_r}\sqrt{\frac{2}{\epsilon_r + 1}}, \tag{22}$$

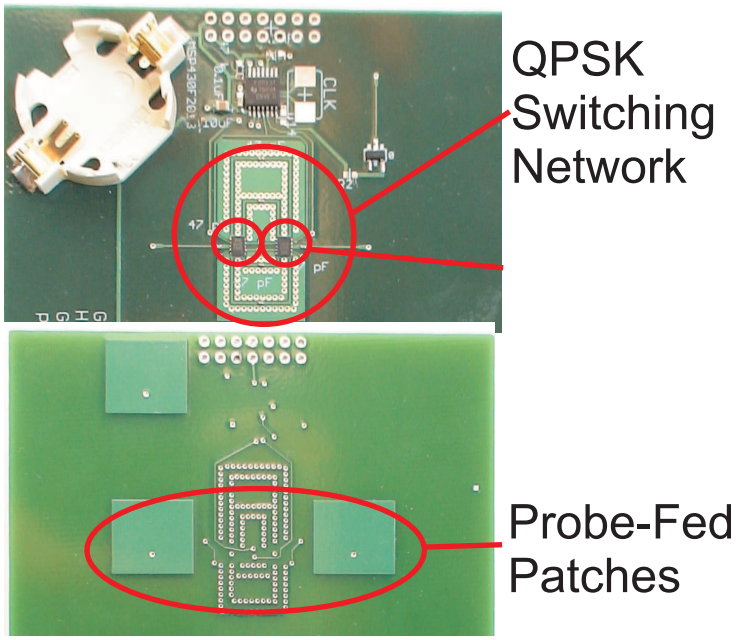

Figure 22: QPSK RAPM prototype on FR-4 with switching network, RF switches, and probe-feed patch antennas.

$$L = \frac{1}{2f_r\sqrt{\epsilon_{\text{reff}}}\sqrt{\mu_0\epsilon_0}} - 2\Delta L, \tag{23}$$

$$\Delta L = h{\cdot}0.412\frac{\left(\epsilon_{\text{reff}} + 0.3\right)\left(\frac{W}{h} + 0.264\right)}{\left(\epsilon_{reff} - 0.258\right)\left(\frac{W}{h} + 0.8\right)}, \tag{24}$$

where W is the patch width, L is the patch length, and h is the separation distance between the patch and its ground plane. These physical dimensions correspond to the probe fed patch antenna shown in Figure 23. Equation (22) was used to calculate the width of the patch, which was dependent upon the relative permittivity of the substrate used. The relative permittivity of the substrate was not straightforward though, since a modified four layer stack-up was used. To increase antenna efficiency, the 2nd metal layer was removed from the 4-layer stackup, as show in Figure 24. In doing so, a three layer board was created, and the spacing between the patch and its ground plane was increased from 10 mils to approximately 50 mils.

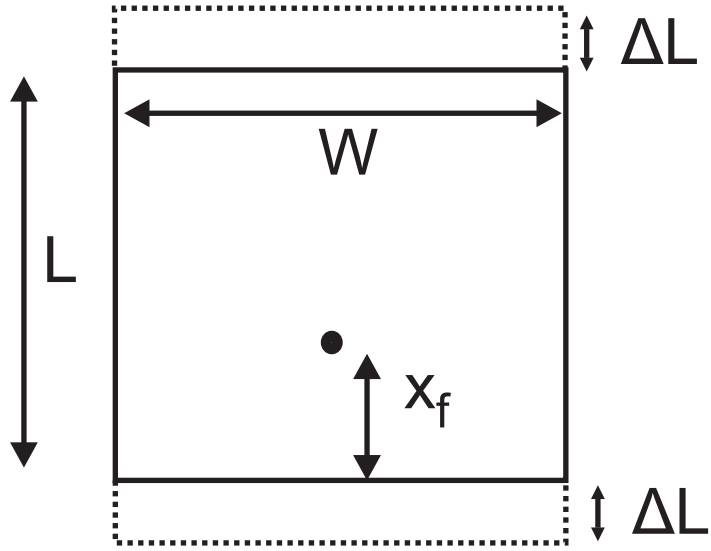

Figure 23: Physical dimensions corresponding with patch design equations.

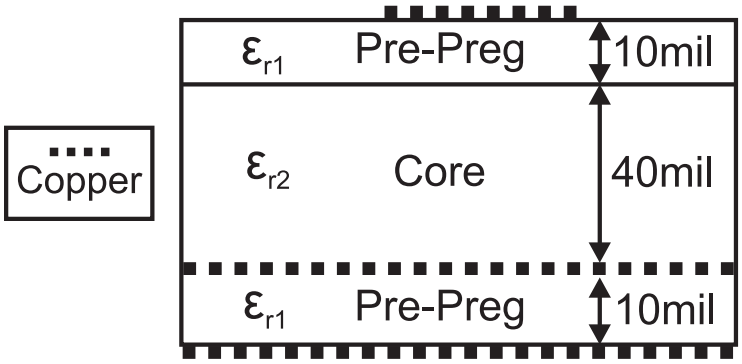

Figure 24: FR-4 stack up used for RAPM design. Second metal layer is removed to provide increased patch to ground separation.

3.1.2 Determining Substrate Permittivity

Due to the removal of the 2nd metal layer, the patch substrate became a combination of the pre-preg material and the core material, creating an effective relative permittivity that was a combination of the two materials. Since the resonant frequency of the patch depends heavily on the relative permittivity values used in the design equations, and defines the relative permittivity used in simulations, it was deemed critical to find the relative permittivities of the substrate materials. Thus, steps were taken to characterize the pre-preg and the core materials individually. The first step in characterizing the substrate was to use 50 Ω microstrip test trace on the bottom layer of the board to determine the effective relative permittivity of the 2116 style pre-preg. By creating a test trace of known length and using a VNA to measure its phase delay, the effective relative permittivity for a microstrip trace was determined from the following equation:

$$\epsilon_{\text{reff}} = \left(\frac{G_D \cdot c}{L_{\text{eff}}}\right)^2, \tag{25}$$

where G_D is the measured group delay, c is the speed of light in a vacuum, and L_{eff} is the effective physical length of the test trace. For arriving at the $L_{physical}$ value, it is important to take into account the VNA calibration technique used, the calibration standards, and the SMA body length. For a short, open, load, and through (SOLT) VNA calibration, L_{eff} can be found by

$$L_{eff} = L_{\text{trace}} + 2 \cdot L_{\text{SMA body}} - L_{\text{barrel}}, \tag{26}$$

where L_{trace} is the physical length of the trace, $L_{SMAbody}$ is the length added by the SMA connector from edge of the board to the tip of the SMA threads, and L_{barrel} is the length of the barrel used for the through calibration, as shown in Figure 25. The relative permittivity of the pre-preg can then be found by backsolving the microstrip effective relative permittivity equation,

$$\epsilon_{\text{reff}} = \frac{\epsilon_r + 1}{2} + \frac{\epsilon_r + 1}{2}\left(1 + 12\frac{H}{W}\right)^2, \tag{27}$$

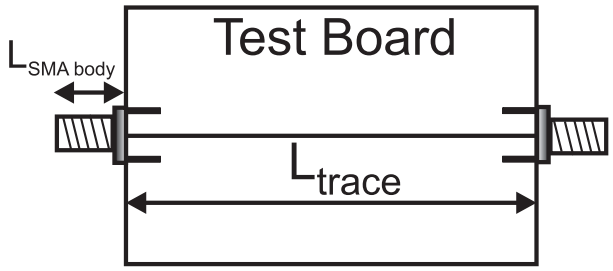

Figure 25: Test board for measuring trace group delay and calculated relative permittivity of board pre-preg.

and to find ϵ_r, where H is the thickness of the pre-preg layer and W is the width of the test trace.

Implementing equations (25) through (27), the relative permittivity of the pre-preg was found to be approximately 3.9. This agrees with the measurements performed by Isola, a leading manufacturer of FR-4 laminates and pre-pregs, who states that the relative permittivity for the 2116 style pre-preg varies between approximately 3.8 and 4 [25].

The relative permittivity of the pre-preg is then combined with the relative permittivity of the core to ascertain the effective substrate permittivity used to calculate the patch's dimensions. To obtain a rough estimate of the effective relative permittivity, the following equation was used:

$$\epsilon_{reff} = \frac{h_{pre-preg}}{h_{total}}\epsilon_{pre-preg} + \frac{h_{core}}{h_{total}}\epsilon_{core}, \tag{28}$$

where $h_{pre-preg}$ is the thickness of the pre-preg layer, h_{core} is the thickness of the core layer, and h_{total} is the sum of the two. For the initial patch calculations, a test trace could not be built directly on the core material to determine its permittivity, so the FR4 standard, IPC 4101/21, value of 4.34 at 1 GHz was used as the initial design value for the core's permittivity [26]. The estimated effective relative permittivity of 4.25, determined from equation (28), was then used in calculating initial patch dimensions.

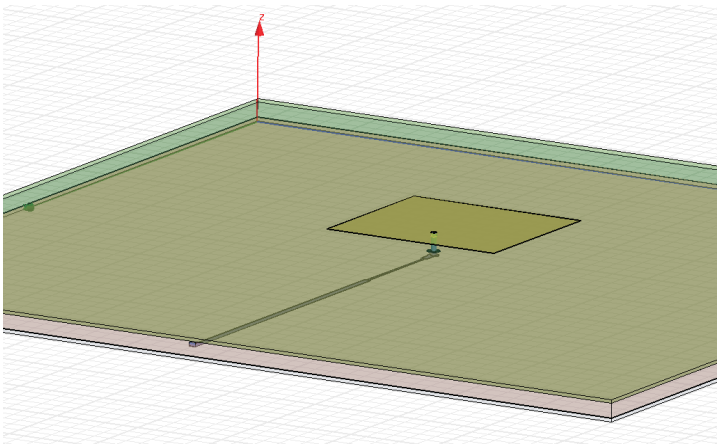

Figure 26: Probe fed patch designed for 3-layer FR-4 stack up.

3.1.3 HFSS Simulation and Feed Location

Based upon the initial patch dimensions of W=1.59 cm and L=1.139 cm, a probe fed patch design, shown in Figure 26, was constructed in Ansoft HFSS and optimizations were performed to center the resonant frequency of the patch about 5.8 GHz. The probe feed, rather than the microstrip feed, was chosen to allow the QPSK switching network to be placed on the bottom layer of the FR-4 stackup. In doing so, the trace to ground spacing is 10 mils rather than 50 mils, decreasing the trace widths, conserving board real estate, and moving parasitic metallic elements further away from the antenna.

3.1.3.1 Antenna Feed

The initial location of the feed, given by x_f,y_f, was calculated using the following equations that approximate the location necessary to achieve a 50 Ω input impedance [27]:

$$x_f = \frac{L}{2\sqrt{\epsilon_{re}(L)}}, \tag{29}$$

$$\epsilon_{re}(L) = \frac{\epsilon_r + 1}{2} + \frac{\epsilon_r - 1}{2} F\left(\frac{L}{h}\right), \tag{30}$$

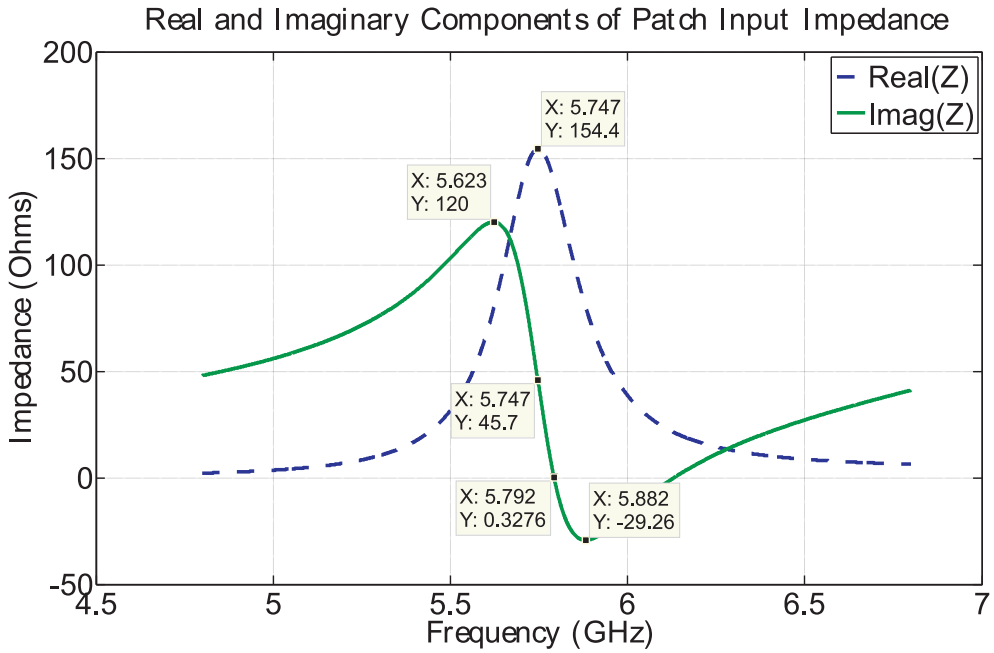

Figure 27: Input impedance of patch using feed equation (29).

$$\text{and} \quad F\left(\frac{L}{h}\right) = \left(1 + \frac{12h}{L}\right)^{\left(-\frac{1}{2}\right)}, \tag{31}$$

where x_f is the feed distance from the edge of the patch. The y_f coordinate of the feed location was chosen to be W/2 in order to suppress higher order TM_{0n} odd modes from being excited. The initial feed location resulting from equations (29) through (31) produced a patch with an input impedance of 154 Ω at the patch's resonant frequency, as shown in Figure 27. Here we can clearly see the 50 ohms of reactance added by the the long feed probe that extends from the patch to the bottom layer of board. As a result of added inductance of the probe feed, the resonant frequency of the loaded patch shifts to 5.792 GHz. The immediate problem however, is that the patch input resistance at resonance does meet the 50 Ω value predicted by equation (29). An investigation into the source of this error led back to the original source of the probe feed location equations, which can be found in [2]. The original paper, in contrast to [27], used a different forcing function than the one listed in equation (31).

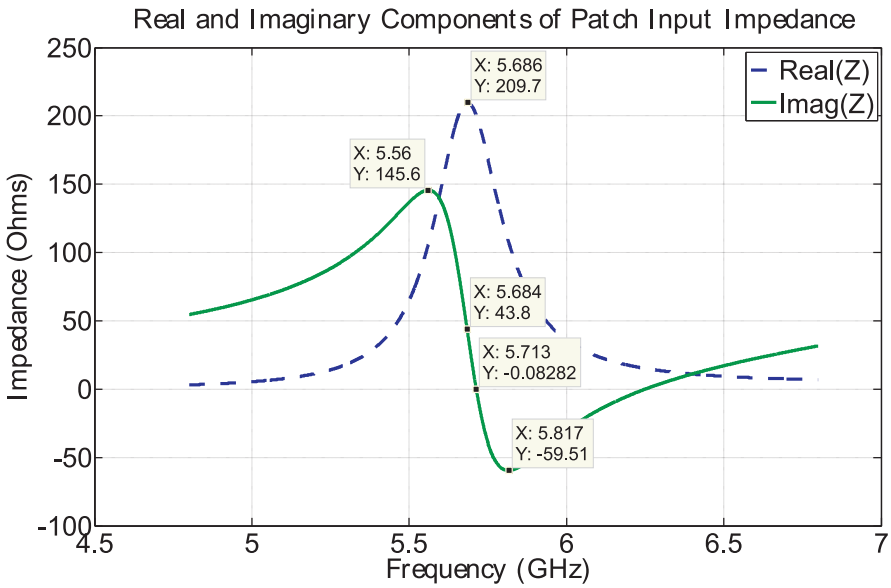

Figure 28: Input impedance of patch using feed equation with original forcing function from[2]

Instead, the forcing function from the original text was:

$$F\left(\frac{L}{h}\right) = \sqrt{1 + \frac{10h}{L}}. \tag{32}$$

After re-simulating the antenna with the updated feed position equation, the peak input resistance for the patch increased to 210 Ω, as shown in Figure 28. Again, this did not approach the expected 50 Ω input resistance published by Kara in [2]. Upon a deeper analysis of Kara's approach for deriving the probe feed position equation, it was realized that Kara's equation was empirical. The author failed to state that this equation only holds over the range of substrate permittivities that were measured. For his 16 measurements, the relative permittivity of his patch substrates varied between 2.22 and 2.55, with one measurement taken with a permittivity of 10.2. To correct the feed location equation, a permittivity scaling factor was added, based upon the belief that the equation should scale according to substrate permittivity. To test this hypothesis, an average permittivity for Kara's 16 measurements was taken, and the average permittivity for these experiments was found to be 2.42. By taking the ratio

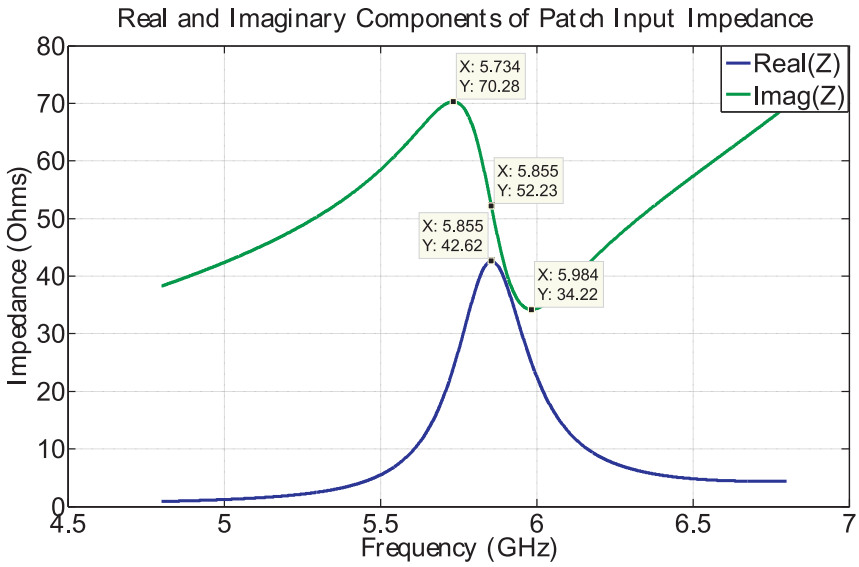

Figure 29: Input impedance of patch using feed equation with original forcing function and new scaled feed position equation.

of this average permittivity to the effective permittivity of the FR-4, the updated feed position equation becomes:

$$x_f = \frac{\epsilon_{eff} L}{2{\cdot}2.423\sqrt{\epsilon_{re}\,(L)}}, \tag{33}$$

To validate this new feed position equation, an HFSS simulation was run with the updated feed location. The resulting patch input impedance is provided in Figure 29. From this Figure, we see that equation 33 provides a peak input resistance of 43 Ω, much closer to the expected input impedance of 50 Ω.

The problem with the antenna feed equations, however, was not realized until after fabrication of the RAPM prototype, thus, the fabricated antenna was based off the incorrect feed position equation given by (29), and a quarter wave transformer was used to match the real part of the resulting antenna impedance at 5.8 GHz from 139 Ω down to 50 Ω in order to provide matching between the antennas and the RF switches.

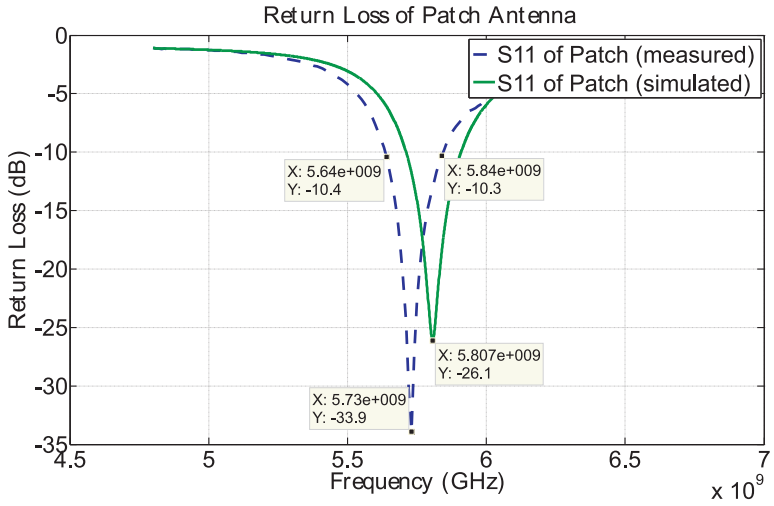

Figure 30: Return loss of measured patch vs simulated patch with $\epsilon_{rcore} = 4.34$.

3.1.4 Antenna Optimization and Prototyping

To improve the performance of the patch, HFSS simulations were performed to minimize the antenna return loss and center it about 5.8 GHz. As optimization parameters, the antenna width and length, as well as the quarter wave transformer width and length were varied until an optimal match was achieved. Based upon the HFSS simulation, the patch demonstrated a return loss of -26 dB at 5.8 GHz, but the fabricated patch demonstrated a resonant frequency of 5.73 GHz and a return loss of -33.9 dB, as shown in Figure 30.

The large difference between the resonant frequency of the simulated and measured patch was found to be the result of an incorrect initial guess at the relative permittivity of the FR-4 core material. Due to the wide variation in resin content of the FR-4 and its respective fiberglass weave, the permittivity of the core material can vary up to 0.5, making the FR-4 permittivity fall anywhere between 4.09 - 4.59, with respect to the 4.34 permittivity value listed by the IPC standard [28]. In addition, moisture absorption in the FR-4 can also induce up to a one percent variation in permittivity. To estimate the actual core permittivity for the fabricated patch, the

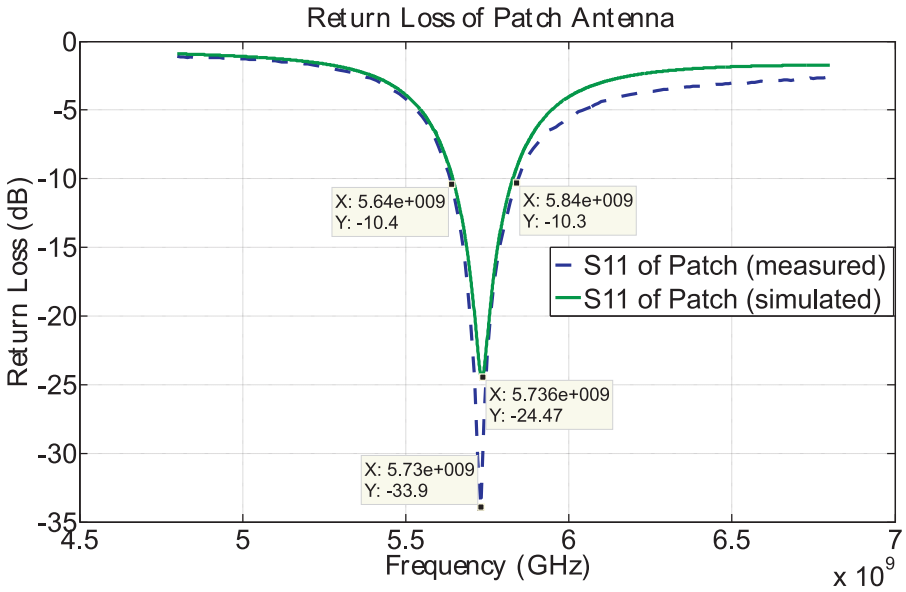

Figure 31: Return loss of measured patch vs simulated patch with corrected $\epsilon_{rcore} = 4.53$ for FR-4 core.

permittivity for the HFSS model was swept from 4.09 to 4.59 until the return loss coincided with the return loss of the fabricated patch. As shown in Figure 31, the simulated patch's return loss coincided with the measured patch's return loss when a relative permittivity of 4.53 was used for the FR-4 core. This is in agreement with the measurements performed by Djordjević, who performed a wideband frequency-domain characterization of FR-4 and found the permittivity to be approximately equal to 4.5 at 5.8 GHz [29].

The final antenna simulation at 5.8 GHz produced a peak gain of approximately 4 dBi, as shown in gain plot of Figure 32. The key antenna parameters for the final antenna have been listed in table 1.

3.2 Switching Network

3.2.1 Microstrip Based Design

The QPSK switching network, shown in Figure 33, was designed using the Agilent ADS LineCalc tool to determine the physical lengths for the $\lambda/4$, $\lambda/2$, $3\lambda/4$, and λ

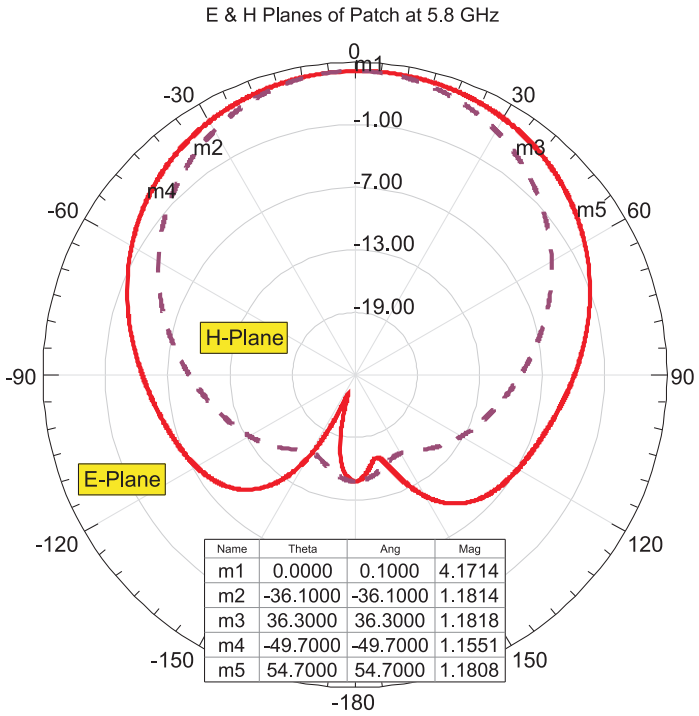

Figure 32: Simulated E and H planes for patch antenna at 5.8 GHz.

Table 1: Patch Antenna Parameters

Antenna Parameters		
Peak Gain	4.17 dBi	Simulated
Resonant Frequency	5.73 GHz	Measured
10dB Impedance Bandwidth	200 MHz (3.4%)	Measured
Horizontal 3dB Beamwidth	72 degrees	Simulated
Vertical 3dB Beamwidth	104 degrees	Simulated
Radiation Resistance	139 Ω (5.8 GHz)	Simulated
Antenna Width	1.283 cm	
Antenna Length	1.165 cm	

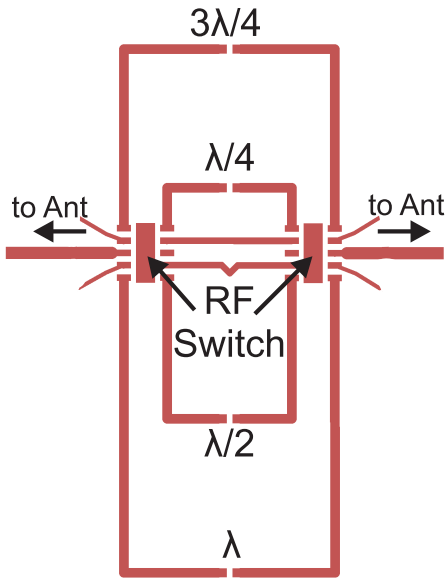

Figure 33: Layout of QPSK switching network used to perform phase shifting of the re-radiated signal.

transmission line sections, based upon the measured pre-preg permittivity of 3.9 and a trace to ground spacing of 10 mils. The initial design was built using a microstrip line topology and Skyworks 13322-375LF single pole four throw (SP4T) RF FET switches, but the phase lengths of the fabricated switching network did not produce the desired relative phase differences of 90 degrees between the $\lambda/4$, $\lambda/2$, $3\lambda/4$, and λ switching segments.

To characterize the switching network, SMA connectors were attached to the two antenna ports of the switching network shown in Figure 33, and an Agilent E5071B VNA was set to zero span, with a center frequency of 5.8 GHz. A microcontroller was then programmed to have the RF switches connect the four transmission line segments in series with the antenna feed, one at a time. By plotting the phase of the S21 measurement versus time, as seen in Figure 34, the relative differences in phase between the switching segments were analyzed. Listed in table 2 are the S21 phases measured as each switching segment was connected to the antenna feed lines by the RF switches.

Table 2: Measured S21 Phase of a Microstrip Switching Network

Phase Lengths		
Line Length	Measured Phase	Relative Phase Difference
$\lambda/4$	78.7°	59.9° (138.6-78.7)
$\lambda/2$	138.6°	112.2° (250.8-138.6)
$3\lambda/4$	250.8°	79.8° (330.6-250.8)
λ	330.6°	108.1° (360-330.6+78.7)

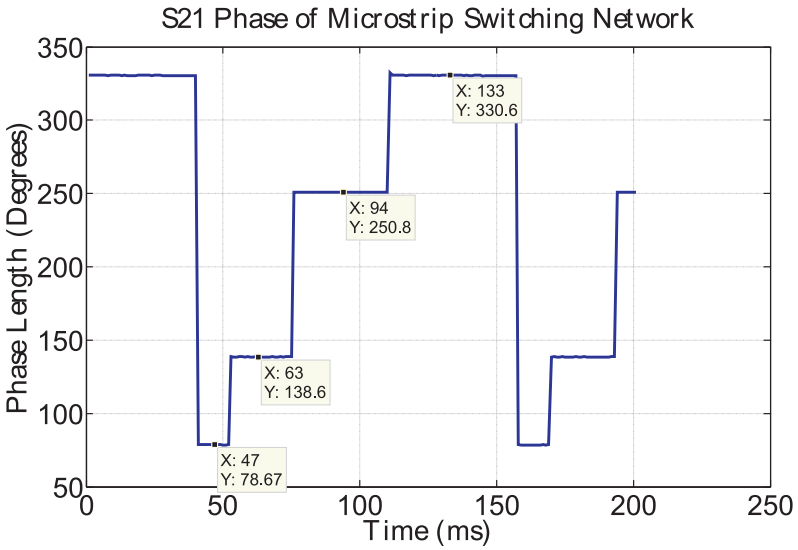

Figure 34: S21 Phase differences between $\lambda/4$, $\lambda/2$, $3\lambda/4$, and λ switching segments of microstrip switching network.

The key metric that determines the phase shifting capabilities of the switching network is the relative phase difference between each switching segment, since this directly determines the distance between states in signal space. For calculating the relative phase difference, the measured phase for a switching segment is compared to next longest segment. For example, the $\lambda/4$ phase is compared to the $\lambda/2$ phase and so on. As shown in table 2, the relative phase difference between the $\lambda/4$ and $\lambda/2$ switching segments was 59.9 degrees, a deviation of 30 degrees from ideal.

The reason for the gross error in phase length was hypothesized to be a result of inhomogeneity of the FR-4, which is known to change permittivity depending upon

Table 3: Measured S21 Phase of a Co-Planar Waveguide Switching Network

Phase Lengths		
Line Length	Measured Phase	Relative Phase Difference
$\lambda/4$	59.6°	57.9°(117.5-59.6)
$\lambda/2$	117.5°	127.3°$(244.8 - 117.5)$
$3\lambda/4$	244.8°	59.7°$(304.5 - 244.8)$
λ	304.5°	115.1°$(360 - 304.6 + 59.6)$

whether a trace runs parallel or orthogonal to the fiberglass weave. Since the traces of the switching network run parallel or orthogonal to the fiberglass weave for different physical lengths, it was assumed that the difference in permittivity introduced by this resulted in unequal variation of phase length for each switching segment. To reduce the dependence of the switching network on the permittivity variations introduced by substrate inhomogeneity and variation in trace to ground spacing, the transmission line topology was changed to co-planar waveguide (CPWG) in order to constrain fields to the substrate surface and reduce the effects of the substrate.

3.2.2 Co-Planar Waveguide Based Design

The S21 phase properties for the CPWG switching network are provided below in table 3.

3.2.3 RF Switch Phase Lengths

The phase differences between switching segments for CPWG case, however, was found to deviate even further from 90 degrees than the microstrip scenario, with the worst case phase difference being 127.3 degrees, a deviation of 37.3 degrees from ideal. From table 3, we see that positive phase deviations occur when switching from the $\lambda/2$ segment to the $3\lambda/4$ segment, and from the λ segment to the $\lambda/4$ segment. Similarly, negative deviations occur when switching from $\lambda/4$ to $\lambda/2$ and $3\lambda/4$ to λ. From table 4, we see that the $\lambda/4$ and $\lambda/2$ segments are connected to ports 1 and

Table 4: RF switch connections of transmission line segments

Connections	
Line Length	Switch Ports
$\lambda/4$	1 & 2
$\lambda/2$	1 & 2
$3\lambda/4$	3 & 4
λ	3 & 4

2, and the $3\lambda/4$ and λ segments are connected to ports 3 and 4 of the RF switch. This led to the initial explanation that the phase deviations were caused by different phase lengths inside the RF switch itself. Physically, the idea is plausible, since the effective electrical wavelength for gallium arsenide is 1.44 cm and the switch package size is 0.4 cm by 0.3 cm. To account for the worst case 37.3 degree phase deviation measured, the transmission lines for ports 1 and 2 would only need to be 0.14 cm shorter than ports 3 and 4, a realistic value. The idea of longer internal transmission lines is further supported by the datasheet for the RF switches, which shows 1 dB more of insertion loss for ports 3 and 4.

To test this hypothesis, a symmetric test board, shown in Figure 35, was fabricated to characterize the phase lengths of each port of the Skyworks switch. A VNA was then used to measure the phase length through each switch port to the common antenna port. The resulting S21 phase measurements, shown in Figure 36, show that only a 3 degree phase difference exists between ports 1, 2, 3, and 4. This leads to the assumption that the phase lengths from each port to the antenna port are equal, with the 3 degree phase difference resulting from PCB manufacturer build tolerances, which resulted in slightly different breakout trace lengths between ports 1,2 and 3,4.

3.2.4 Reflections and Additional Phase Shifts

The next hypothesis for why the switching network did not achieve 90 degree phase differences is based upon the idea that impedance mismatches between the switching

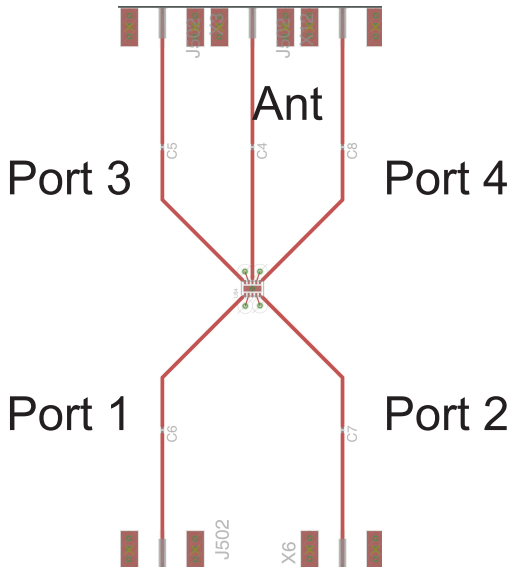

Figure 35: Skworks switch test board.

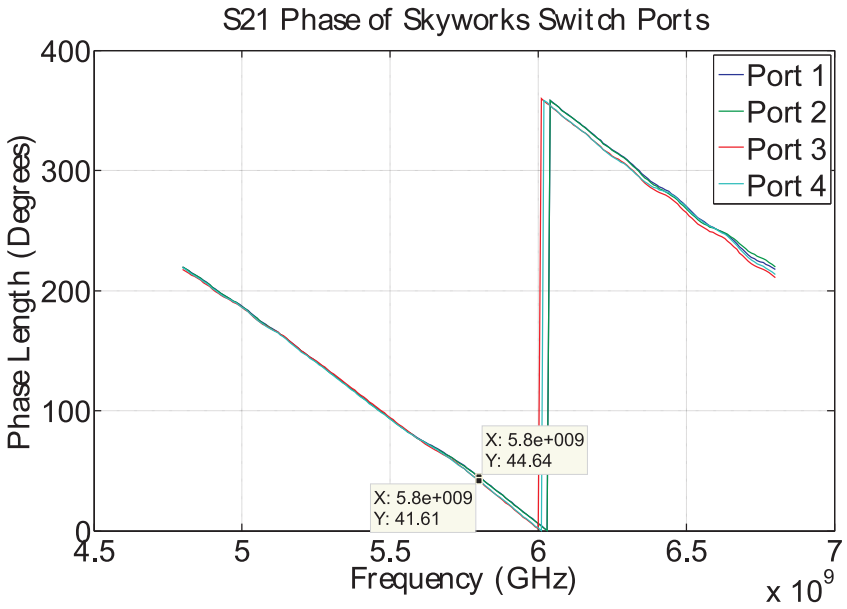

Figure 36: S21 phase measurement between each port and the antenna port of a Skyworks RF switch.

segments and RF switches led to reflections that changed the amplitude and phase of the forward traveling wave. This concept is depicted in Figure 37 and was derived from the theory of infinite reflections as:

$$V_{total}^{+} = \sum_{n=0}^{\infty} V^{+} e^{-jn\beta 2l} \left(\Gamma_{for} - \Gamma_{back}\right)^{n}, \tag{34}$$

where V^{+} is the magnitude of the main unreflected component of the forward traveling wave and is defined to have zero phase and unity amplitude at the reference plane shown in Figure 37. The $e^{-jn\beta 2l}$ term then represents the phase shift that occurs as a reflected wave is generated at the reference plane, propagates back toward the switch on the right, and is reflected back to the reference plane. The remaining Γ_{for} and Γ_{back} terms represent the reflection coefficients seen looking from each switching segment into its respective switch ports.

Equation 34 therefore defines the total forward traveling wave, V_{total}^{+}, with respect to the reference plane defined in Figure 37 and is a function of switching segment length and the reflection coefficients associated with each respective switching segment. Yet, in order for forward traveling reflections to change the phase of V_{total}^{+} in a QPSK switching network, the reflection coefficients must be complex. Since the switching segments are integer multiples of a quarter-wavelength, all reflections arrive back at the reference place with phase shifts of integer multiples of 180 degrees, since purely real reflection coefficients only change the magnitude of a reflection or invert its phase. As a result, the forward traveling reflections arrive back at the reference plane completely in phase or out of phase with respect to the unreflected component, V^{+}, and change its magnitude, not its phase. With complex reflections coefficients, however, additional phase shifts are induced in the reflections at the point of an impedance mismatch, causing them to arrive at the reference plane with a phase different to that of V^{+} and creating a new total forward traveling wave, V_{total}^{+}, with a shifted phase.

To investigate the reflection coefficients between the RF switch and the board

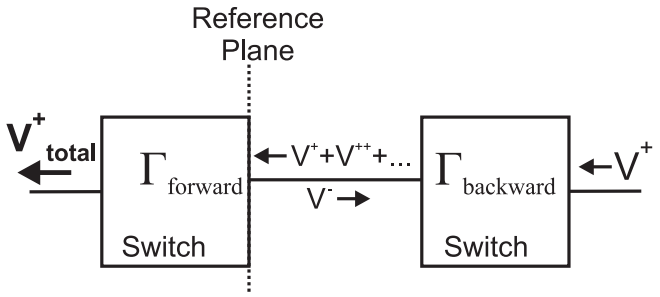

Figure 37: Forward going wave with reflections created by RF switch, transmission line impedance mismatches.

traces, the switch test board was used to characterize the S11 properties of each switch port. As shown in Figure 38, the return losses for ports 1, 2, 3, 4, and the antenna port are: -9.7 dB, -9.2 dB, -7.9 dB, -7.4 dB, and -11.8 dB, respectively. Since the breakout traces for each port are of equal length and symmetry, these differences in return loss result due to different reflection coefficients between the board trace and switch input ports. Converting the S11 measurements to reflection coefficients, it becomes obvious that the reflections generated by the trace-to-switch impedance mismatches are of significant amplitude, as shown in Figure 39.

The critical question, however, is whether or not the phase changes produced by the impedance mismatches are different for each switching segment, since different phase changes are necessary to explain the phase deviations measured for the CPWG switching network. If measured phase for the S11 of each switch input was the same, it would mean that all ports have equal reactance and that the phase of V^+_{total} would change equally across the four switching segments, thereby maintaining 90 degree phase differences between segments. This was not to be expected though, since the fabricated QPSK switching network did not achieve 90 degree phase differences. Instead, the phase of S11 and the reactance of each RF switch port was expected to vary from port to port.

Shown in Figure 40, the measured S11 phases for ports 1, 2, 3, and 4 were found

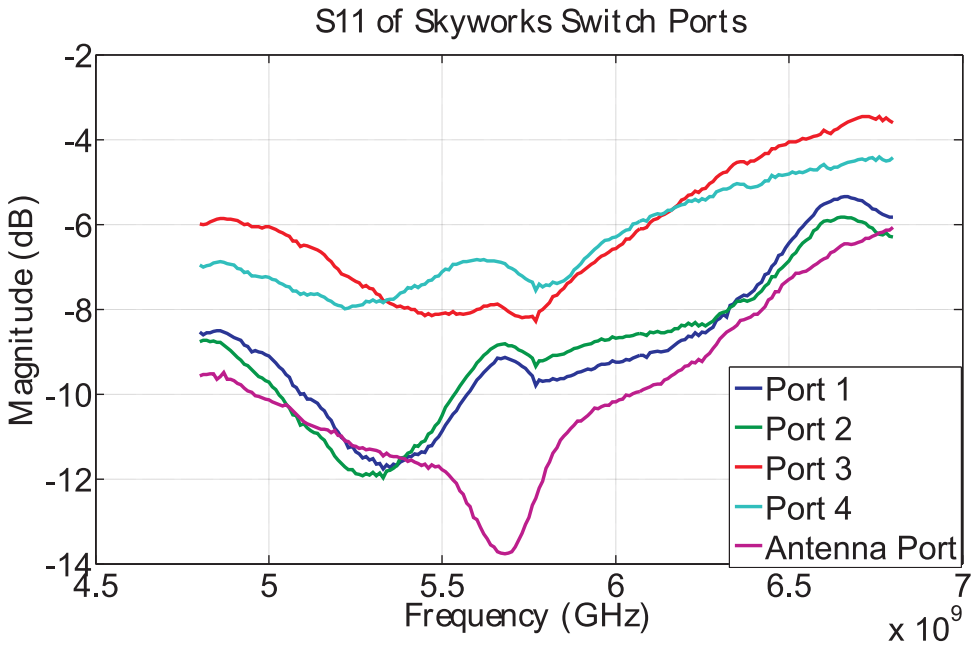

Figure 38: Magnitude of S11 parameters for each port of the RF switch.

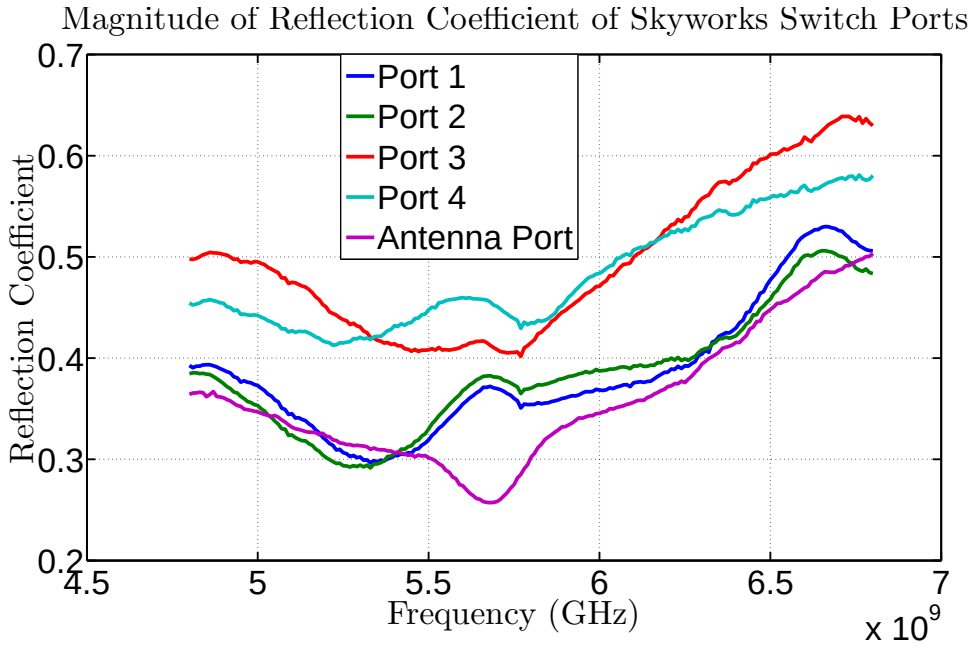

Figure 39: Reflection coefficients between switch ports and feed traces.

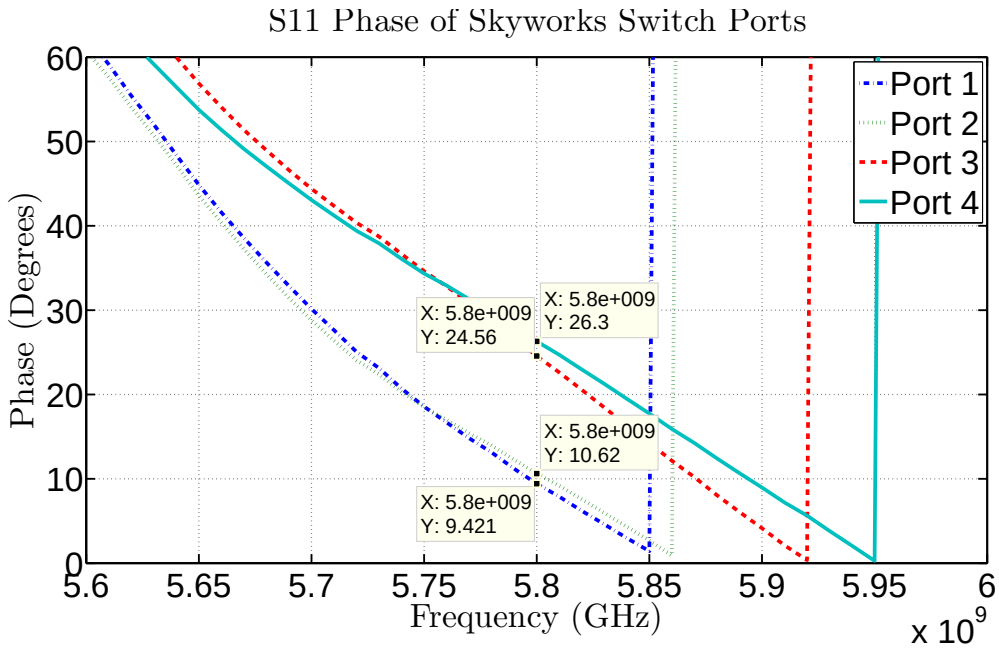

Figure 40: S11 phase of ports for Skyworks switch mounted on test board.

to be: 9.4°, 10.6°, 24.6°, and 26.3°, respectively. This variation in S11 phase is attributed solely to the complex reflection coefficients of the switch ports, since the breakout traces on the test board are of equal length. Furthermore, since ports 3 and 4 produce approximately 15 degrees more of phase shift in their S11 measurements, these ports are inherently more reactive than ports 1 and 2. The different phases of the S11 measurements can then be directly correlated with the measured relative phase differences of the CPWG switching network.

To validate the theory that complex reflections coefficients are creating the phase deviations in the QPSK switching network, a simulation was performed in Matlab using equation (34) to calculate the magnitude and phase of the cumulative forward traveling wave, V^+_{total}, at the output of the switching network. Using the topology shown in Figure 37, the input port to the second RF switch on the left was established as the zero degree reference plane for the main, non-reflected, forward traveling wave, V^+. The S11 measurements of the RF switch ports were then used to backsolve for the input reactance, X_{in}, of each RF switch port. Using the magnitude of the

reflection coefficient, given as:

$$|\Gamma| = \left| \frac{Z_{in} - Z_0}{Z_{in} + Z_0} \right|, \tag{35}$$

where the Z_{in} and Z_0 terms represent the input impedance of the switch port and the characteristic impedance of the CPWG traces. To backsolve for X_{in}, the measured S11 values were first converted to linear reflection coefficients. The Z_{in} term was then set to $50 + jX_{in}$ Ω, and the Z_0 term was set to $50 + j0$ Ω. Equation (35) was then solved to determine the X_{in} term. The calculated X_{in} was then substituted into the standard reflection coefficient equation to regain the complex reflection coefficient. These complex reflection coefficients were then substituted into equation (34) to determine the V^+_{total} component generated by each switching segment. The resulting V^+_{total} components were then plotted with respect to the zero phase V^+ component in order to determine the phase shifts induced by the complex reflection coefficients. The original assumptions for the switch and trace impedances, however, did not produce a great enough phase change in the V^+_{total} waves. To approach a solution that modeled the measured phase differences of the CPWG QPSK switching network, the R_0, X_0, and measured reflection coefficient terms were varied to create new X_{in} terms for the reactances of the RF switch input ports.

The final values used in calculating the V^+_{total} wavefront are listed in table 5. Analyzing these final values, we seen that the input impedance of the switch ports is inductive. One explanation for this is that during RF switch design, inductive stubs are built into the device to balance the junction capacitance of the FETs. Since the inductive stubs cannot be designed to give a conjugate match over the entire operational frequency range of the switch, it is expected that the switch input impedance be capacitive or inductive at some frequencies. At 5.8 GHz, the switch reactances calculated by the Matlab simulation correspond to inductance values ranging from 1.6 nH to 2.03 nH.

The resulting phases of the V^+_{total} wavefronts that propagate out of the switching

Table 5: Values used for simulating V^+_{total}

Variables	
Variable	Value
R_{in}	50 Ω
$X_{in}(port1)$	59.9 Ω
$X_{in}(port2)$	62.5 Ω
$X_{in}(port3)$	70.3 Ω
$X_{in}(port4)$	74.0 Ω
R_0	52 Ω
X_0	5 Ω
Γ_{port1}	0.45
Γ_{port2}	0.47
Γ_{port3}	0.42
Γ_{port4}	0.43

network have been plotted in Figure 41 to demonstrate the phase shifting that occurs on the $\lambda/4$, $\lambda/2$, $3\lambda/4$, and λ switching segments. With respect to the unreflected forward traveling component, V^+, the $\lambda/4$, $\lambda/2$, $3\lambda/4$, and λ switching segments produce V^+_{total} wavefronts with phase shifts of: -11.35°,10.03°,-15.44°,-14.11°. From this result, the phases of the V^+_{total} waves of $\lambda/4$ section and the $3\lambda/4$ section are retarded with respect to the V^+ component, making these sections appear physically longer. In the same manner, the $\lambda/2$ and λ sections advance the phase of the V^+_{total} wavefront, making them seem physically shorter. The effective phase length for each simulated switching section is then be found by taking their ideal lengths of 90, 180, 270, and 360 degrees and adding the phase changes created by the reflections. The effective switching segment phase lengths become:

Table 6: Measured vs. Simulated Relative S21 Phase Differences of a Co-Planar Waveguide QPSK Switching Network

Phase Lengths			
Segment Transition	Measured Relative	Simulated Relative	Percent Error
	Phase Difference	Phase Difference	
($\lambda/4$ to $\lambda/2$)	57.9°	68.6°	18.5%
($\lambda/2$ to $3\lambda/4$)	127.3°	115.5°	9.3%
($3\lambda/4$ to λ)	59.7°	60.45°	1.3%
(λ to $\lambda/4$)	115.1°	115.46°	0.3%

$$\begin{aligned} \lambda/4 &= 90^\circ + 11.35^\circ = 101.35^\circ \\ \lambda/4 &= 180^\circ - 10.03^\circ = 169.97^\circ \\ \lambda/4 &= 270^\circ + 15.44^\circ = 285.44^\circ \\ \lambda/4 &= 360^\circ - 14.11^\circ = 345.89^\circ. \end{aligned} \tag{36}$$

These simulated results are compared to the measured S21 phase lengths of the QPSK switching segments in table 6 to ascertain the accuracy of the simulation. We can clearly see that the simulation accurately predicts the effective phase lengths of the switching segments, thereby supporting the belief that complex reflection coefficients are of substantial magnitude and are the root cause for why the prototyped QPSK switching network does not achieve ideal 90 phase differences. Furthermore, this analysis serves as a reminder that the complex input impedance for each port of an RF switch must be characterized, and that for large values of input reactance, matching techniques must be implemented to create real reflection coefficients and eliminate undesired phase shifting.

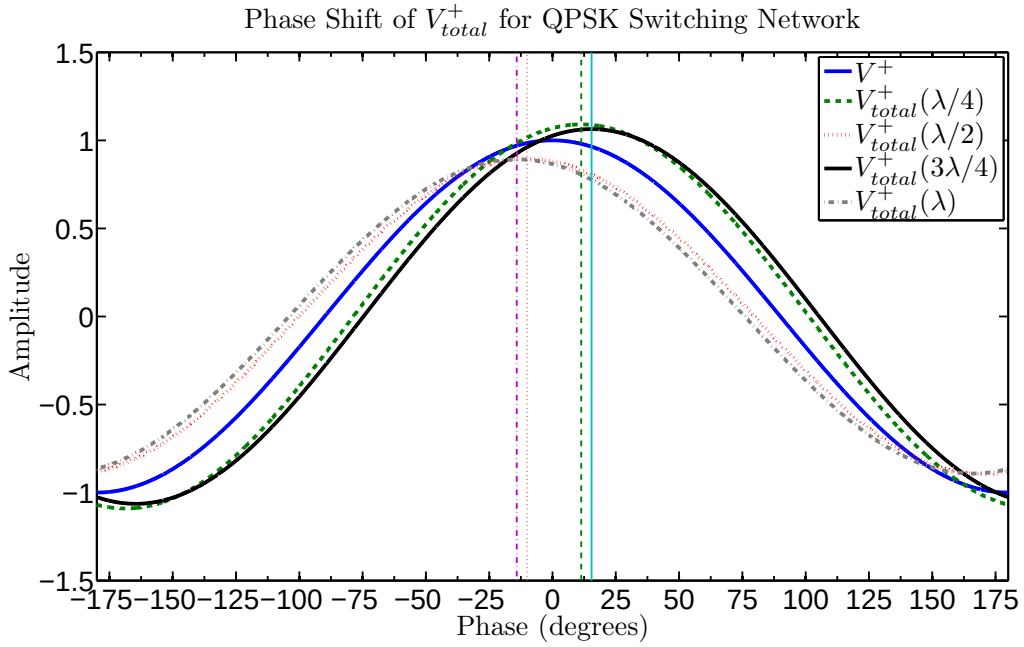

Figure 41: Simulated phase of V^+_{total} for each switching segment with respect to V^+.

CHAPTER IV

RAPM MEASUREMENT SETUPS

4.1 Experiment Setup

4.1.1 Measuring Power Consumption

The setup used for power consumption measurements is shown below in Figure 42. An HP E3631A DC power supply was set to a 3.3 V output, and the positive lead was connected to the positive voltage input of the RAPM. An HP 34401A digital multimeter was then connected in series between the grounds of the RAPM and DC supply to measure series current flow.

4.1.2 Measuring the Backscatter Signal Constellation

The measurement of the RAPM's backscatter signal constellation was performed in room E560 of the Van Leer Building on the Georgia Tech Atlanta campus. The measurement setup is shown in Figure 46. A bistatic collocated setup was implemented on the interrogator side. An Agilent E8247C signal generator was used to feed a -3dBm 5.8 GHz signal into a Mini-Circuits ZVE-8G power amp and the local oscillator (LO)

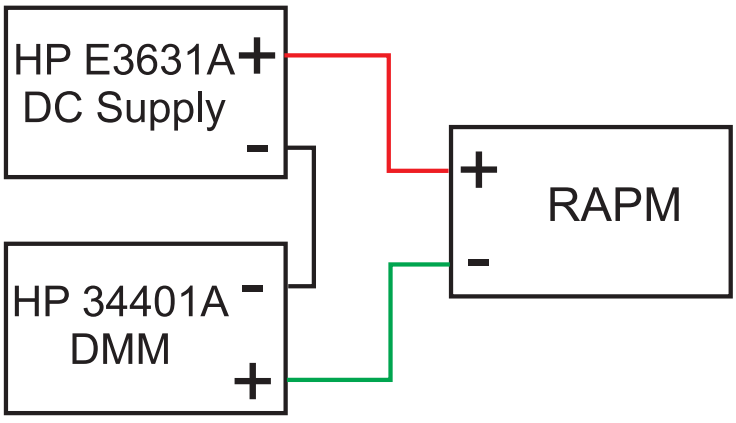

Figure 42: Measurement setup for characterizing RAPM power consumption.

input of a custom homodyne receiver. The interrogator implemented 8 dBi patch antennas with 0.3 m of physical separation. The antennas were enclosed in a tower and covered by radomes as shown in Figure 47. The receive antenna and transmit antennas were at a height of 1.5 m and 1.2 m, respectively. The RAPM was placed 1 meter away from the interrogator antennas and was at a height of 1.5 m.

A custom antenna mount, shown in Figure 48, was constructed to allow for objects to be placed in the anterior and posterior regions of the RAPM. For near-object RAPM measurements, the materials listed in Table 11 were used. For the posterior measurements, the RAPM was placed in the forward most slot of the antenna mount and copper, aluminum, and plexiglass were placed in slots 1 and 2 to vary the tag-to-object separation distance between 9 mm and 30mm, or 0.17 λ and 0.58 λ, respectively. The plywood was attached to the back of the antenna mount, as shown in Figure 43, with a separation distance of 0.93 λ, and the anti-freeze, steak, and distilled water were placed in ziploc bags, attached to a sheet of plexiglass, and placed in slot two, as shown in Figure 44. For the anterior measurements, the RAPM antenna mount was rotated 180 degrees and the RAPM was placed in the rearmost slot and materials were placed in the forwardmost slot. For anterior measurements, materials were placed to block half of the RAPM or the entire RAPM from the interrogator, as shown in Figure 45.

The RAPM was programmed to continuously transmit a QPSK signal at a symbol rate of 1MHz. The signal states were switched in order of phase, from $\lambda/4$ to λ. In order to determine which phase states corresponded with a specific switching segment, the duration of transmission for the $\lambda/4$ state was double that of other states. The received backscatter signal was converted to baseband by a homodyne receiver and transferred to an Exacq CH-3150 2 channel 12-bit ADC. The ADC was set to a sample rate of 20 MHz and a capture window of 10 ms. The data was then imported into Matlab for post processing.

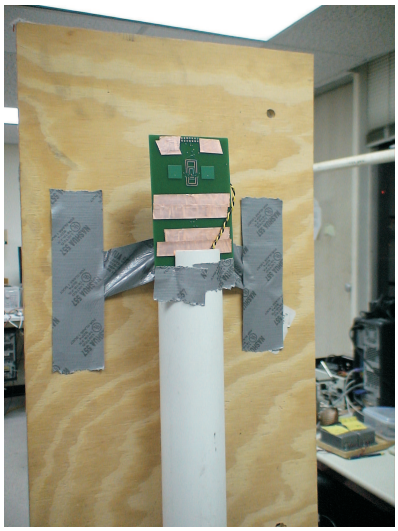

Figure 43: Plywood mounted to the back of the RAPM antenna mount for a posterior measurement.

Figure 44: Anti-freeze, steak, and distilled water mounted on plexiglass and inserted in slot two of RAPM antenna mount for posterior measurements.

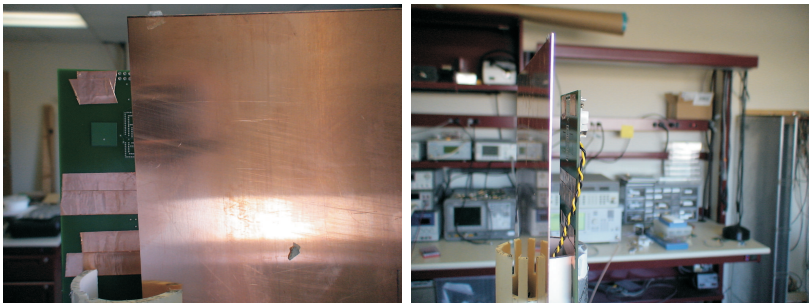

Figure 45: Anterior measurement setup for RAPM antenna mount. Left: half blockage. Right: full blockage.

Table 7: Materials placed in the posterior and anterior regions of the RAPM during backscatter signal constellation measurements

Material	ϵ_r	$\tan(\delta)$	dimensions (in)
Copper	1.0	0.0000	7.5 X 5.75 X 0.02
Aluminum	1.0	0.0000	10 X 7.5 X 0.13
Plywood (Pine)	1.5	0.0220	12 X 22 X 0.45
Plexiglass (Acrylic)	2.6	0.0057	12 X 9 X 0.096
Anti-Freeze	12	1.0000	10 X 5 X 1.14
Steak	40	0.3000	7.5 X 6.5 X 0.39
Distilled Waster	76.7	0.1570	10 X 8 X 1.18

*Values measured at 3 GHz, taken from [30].

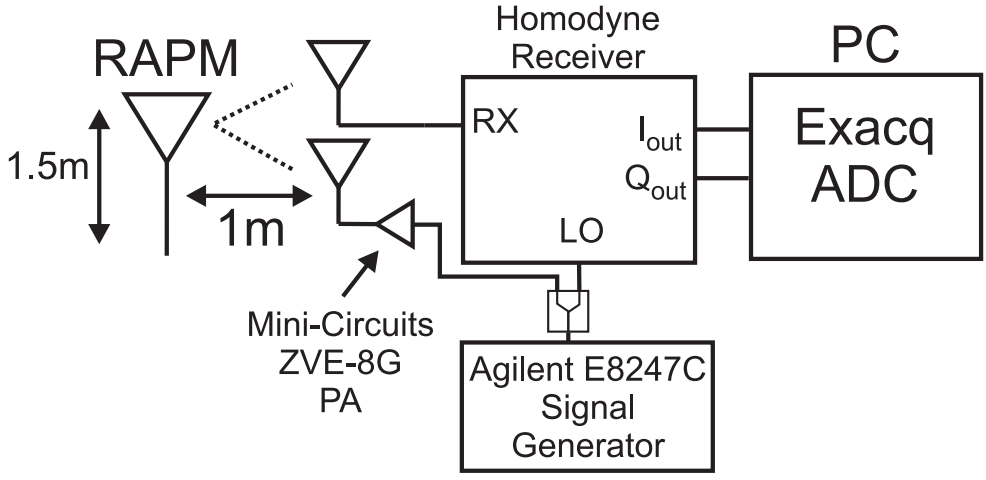

Figure 46: Measurement setup for characterizing the RAPM's backscatter signal constellation.

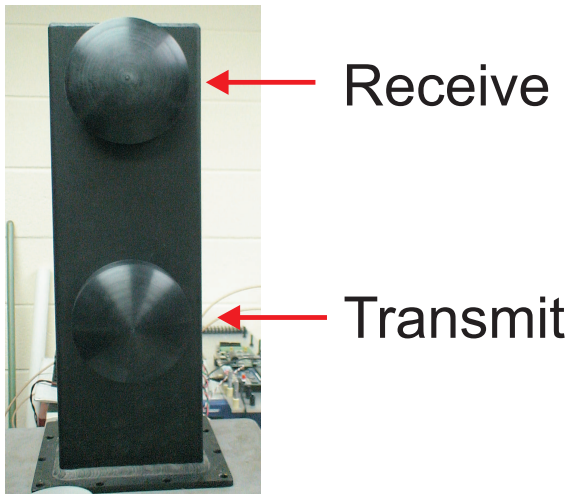

Figure 47: Transmit and Receive antennas on interrogator side. Top: Receive. Bottom: Transmit.

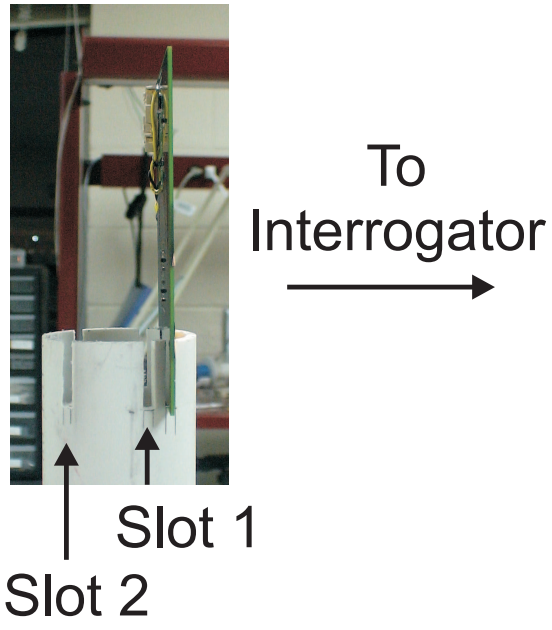

Figure 48: Custom antenna mount for RAPM with slots for object placement.

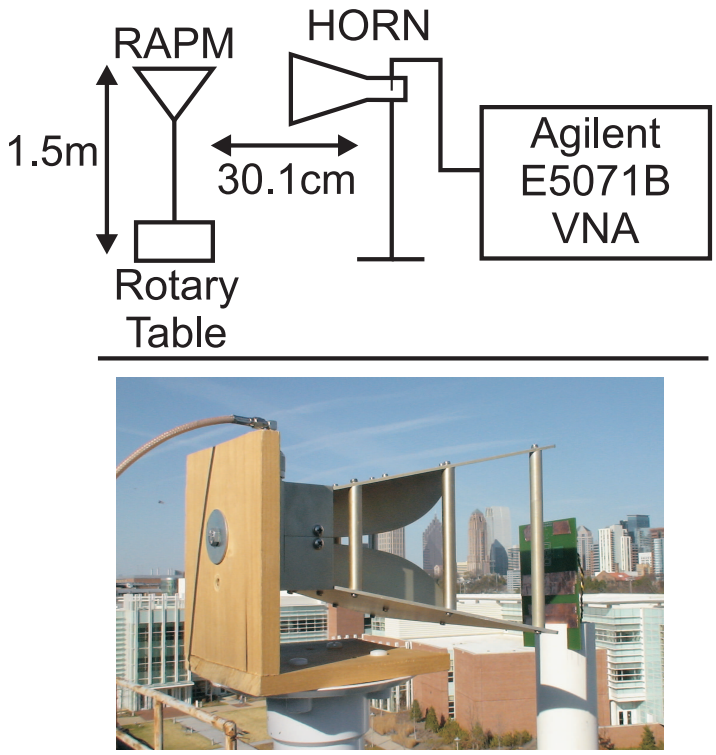

Figure 49: Single-port VNA setup for measuring the radar cross section of a RAPM.

4.1.3 Measuring Radar Cross Section

The radar cross section (RCS) of the RAPM was characterized using the single-port VNA measurement technique proposed by Nikitin in [8]. The measurement system, shown in Figure 49, was constructed on the north east corner of the roof of the Van Leer building to reduce the number of environmental scatterers. The horn antenna was connected to port 1 of an Agilent E5071B with a port output power of 5 dBm. The horn and RAPM were mounted at a height of 1.5 m and separated by a distance of 30.1 cm. The RAPM was placed in its custom antenna mount and attached to a VELMEX 4800 series rotary table. The rotary table was then used to vary the scan angle from -90 degree to +90 degrees, with 0 degrees being broadside incidence and -90 and +90 being end-fire positions.

The measurement procedure involved performing a VNA SOLT calibration at the input to the horn antenna. The feed cable was disconnected from the horn and

the calibration was performed to remove the losses associated with the cable and connectors. The VNA was then set to measure linear S11 magnitude at 5.8 GHz, and a reference measurement was performed as the antenna mount was swept from -90 to +90 degrees without a RAPM present. This measurement was then used to perform background subtraction on RCS measurements with a RAPM present. By subtracting the reference measurement from the RAPM measurements, only RCS changes produced by the RAPM remained.

4.1.4 Measuring the Antenna Mode

Common RCS and radiation pattern measurement techniques cannot separate the structural and antenna modes of an antenna. As a result, for antennas such as a patch, the large structural component created by the patch's ground plane dominates the much smaller antenna mode of the patch. In order to measure the antenna mode, the signal constellation measurement setup is used to filter the unmodulated structural mode created by the RAPM's ground plane. The RAPM was programmed to transmit QPSK at a symbol rate of 1MHz and was swept over a scan angle range of -90 to +90 degrees. Note that the structural RCS does become time varying since the RAPM is rotating, but since the full scan angle sweep duration is eight seconds, the frequency of the structural variation falls well below the 32 kHz cutoff created by 0.1 μF DC blocking caps inside the homodyne receiver.

CHAPTER V

RESULTS

5.1 Power Consumption

Since the RAPM architecture is microcontroller driven, its power consumption is strongly correlated with the microcontroller duty cycle, which is defined as the ratio between time spent in active mode and sleep mode. As the number of bits per symbol increases, the raw bitrate can be held constant while the symbol rate is decreased, thereby reducing transmission time and allowing the microcontroller to spend more time in sleep mode. While not executing processes or transmission instructions, the TI MSP430F2013 microcontroller entered low power mode three as a sleep state, consuming 2.4 μW at 3.3 V. A low power timer onboard the microcontroller was set to periodically wake the microcontroller and place it in an active mode clocked at 16 MHz. During these active cycles, the microcontroller would execute dummy instructions to simulate computation and then execute instructions to control the RF switches and transmit a packet of 20 bits. To vary the number of dummy instructions, two active modes were used for testing power consumption: mode one implemented 20 dummy instructions and mode two implemented 60 dummy instructions.

The ratio of transmission time to processing time is given as,

$$\frac{\text{number of instructions for packet transmission}}{\text{number of instructions for processing}}, \tag{37}$$

where the number of instructions for packet transmission is given as,

$$\frac{\text{bits per packet}}{\text{bits per symbol}}. \tag{38}$$

Thus, by varying the number of dummy instructions, the two different modes allowed us to determine if the ratio between processing time and transmitting time affected

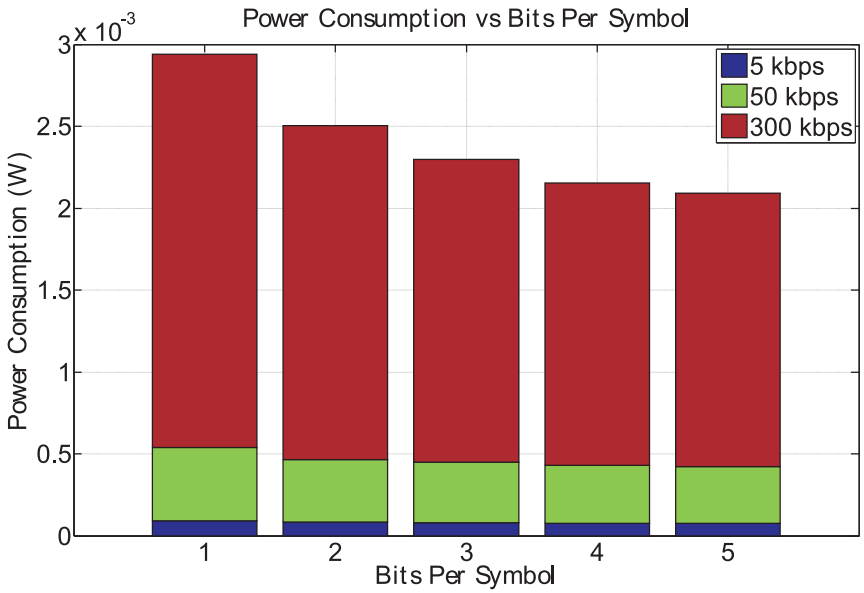

Figure 50: Power consumption of RAPM versus bits per symbol and raw bitrate.

power consumption. In addition to varying the processing time per active cycle, the number of bits per symbol were varied between 1, 2, 3, 4, and 5 to simulate BPSK, QPSK, 8-PSK, 16-PSK, and 32-PSK RAPM implementations. The raw bitrate was then also varied between 5 kbps, 50 kbps, and 300 kbps to determine how raw bitrate affected power consumption.

Shown in Figure 50 is the power consumption of the RAPM under mode one. As we can see, the power consumption decreases for all three raw bitrates as the number of bits per symbol is increased. From Table 8, we see that the decrease in power consumption is strongly linked to raw data rate, with the most prominent decrease in power consumption occurring with a raw bit rate of 300 kbps. Contrasting the power consumption when moving from one bit per symbol to two bits per symbol, we see that for a bitrate of 5 kbps, there is a 9.5 percent decrease in power consumption, but for the 300 kbps case, there is a much greater 15.6 percent decrease in power consumption. This leads to the conclusion that the RAPM benefits more from an increased number of bits per symbol as the raw data rate increases.

Table 8: Decrease in microcontroller power consumption versus symbol rate and raw bitrate for 20 dummy instructions per active cycle.

Bits Per Symbol	5 kbps	50 kbps	300 kbps
1	0%	0%	0%
2	-9.5%	-14.2%	-15.6%
3	-12.4%	-17.9%	-22.9%
4	-15.0%	-21.6%	-28.1%
5	-16.0%	-23.1%	-30.4%

Table 9: Decrease in microcontroller power consumption versus symbol rate and raw bitrate for 60 dummy instructions per active cycle.

Bits Per Symbol	5 kbps	50 kbps	300 kbps
1	0%	0%	0%
2	-8.0%	-9.4%	-12.8%
3	-9.3%	-11.9%	-16.8%
4	-12.0%	-13.9%	-19.7%
5	-13.3%	-14.8%	-20.9%

For the case of mode two, with 60 dummy instructions, the RAPM was found to benefit less from increasing the number of bits per symbol. From table 9, we see that when the number of bits per symbol is increased from 1 to 2, only a 12.8 percent decrease in power consumption occurs for a raw bitrate of 300 kbps. In comparison to mode one, the decrease in power consumption is 2.8 percent less. This negative effect produced by increasing the number of processing instructions becomes even more pronounced as the number of bits per symbol is increased. For the case where there are five bits per symbol, mode one yields a power consumption decrease of -30.4%, whereas mode two yields a lesser decrease of only -20.9%. Therefore, the ratio between RAPM packet transmission time to processing time becomes a key figure for determining power consumption efficiency and emphasizes that microcontroller processing time must be minimized to increase system performance.

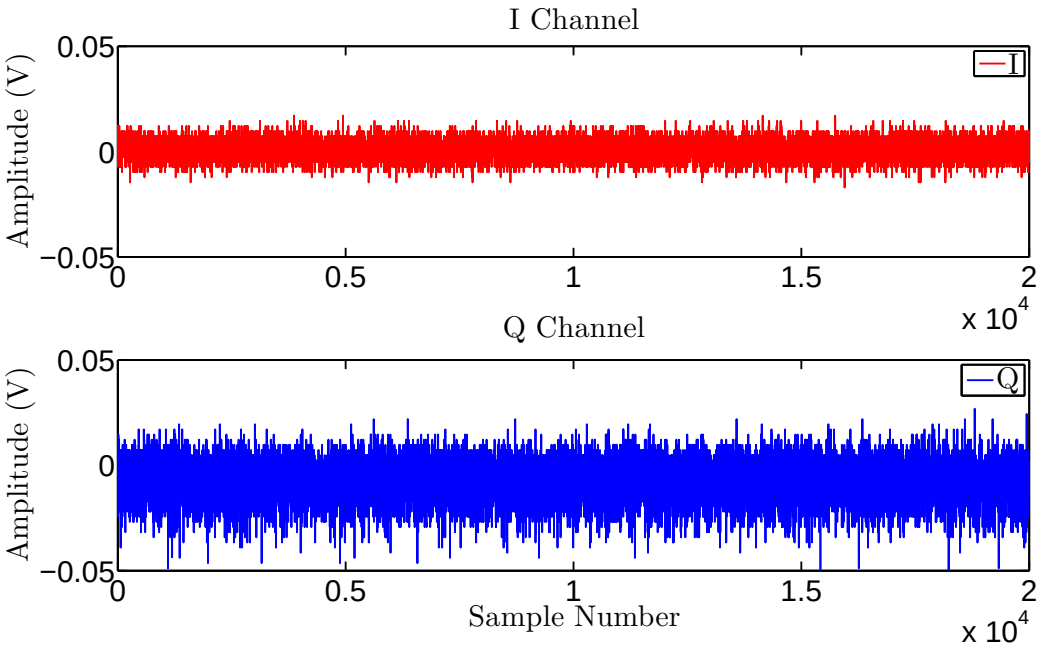

Figure 51: Sampled I and Q voltage outputs of the homodyne receiver with no RAPM present, system noise only.

5.2 Signal Constellation

To characterize the backscatter signal constellation, the sampled I and Q channels were plotted in the complex plane. To center the signal constellation, the I and Q channels were sampled with no RAPM present to determine any DC offsets present. The raw I and Q channels, shown in Figure 51, were then averaged over a window of 10 ms to determine the DC offsets of the homodyne receiver. The DC offsets were found to be 0.78 mV and -7.3 mV for the I and Q channels, respectively. These offsets were then subtracted from the I and Q channels to zero center all backscatter signal constellation measurements .

Between each near-object backscatter measurement, a free space measurement was taken to serve as reference for constellation warping, shrinking, or expansion. An example free space RAPM QPSK signal constellation is shown in Figure 52, where states 0, 1, 2, and 3 represent the phase of the backscattered signal created

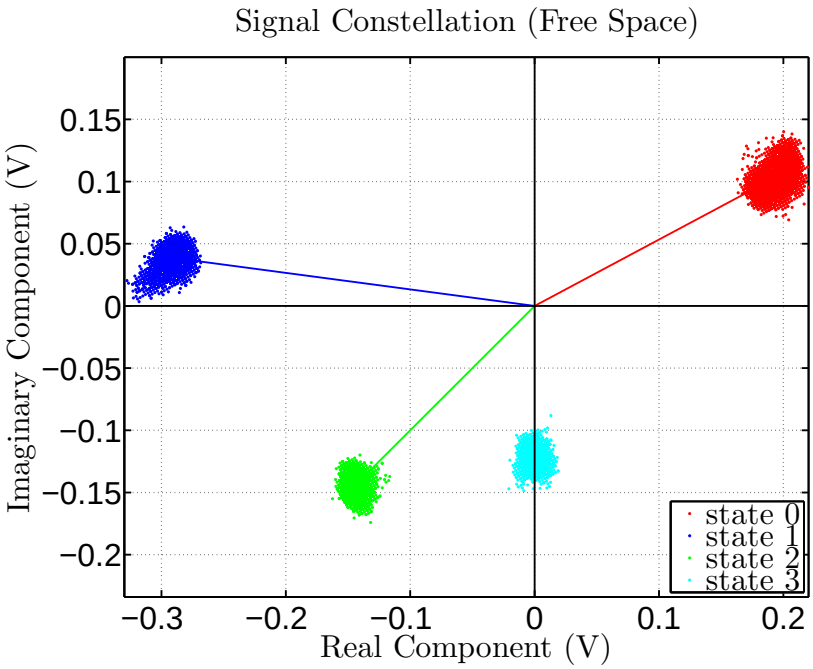

Figure 52: RAPM backscatter QPSK signal constellation (Free Space).

Table 10: Free Space backscatter signal properties of a RAPM.

State	Magnitude (V)	Phase	Relative phase between states
State 0	0.22	28.1°	(0,1) 144.3°
State 1	0.29	172.4°	(1,2) 52.6°
State 2	0.20	225.0°	(2,3) 45.0°
State 3	0.12	270.1°	(3,0) 118.3°

by the $\lambda/4$, $\lambda/2$, $3\lambda/4$, and λ switching segments, respectively. For this free space measurement, the magnitude and phase of each constellation point, with respect to the origin, is listed in table 10. Note that variations in magnitude are rounded to the second decimal place, and variations in phase are rounded to the first decimal place. These significant figures were selected based upon the worst case ADC quantization noise voltage. For the Exacq ADC, with an input voltage range of -5 V to + 5V and 12-bit quantization, the voltage resolution becomes 2.44 mV. The equation defining this voltage resolution can be defined as

$$\text{ADC Voltage Resolution} = \frac{Vref_{pk-pk}}{2^N}, \tag{39}$$

where N is the ADC's resolution in bits. This voltage resolution, also known as the least significant bit (LSB) value of the ADC, then defines the max quantization error, given as,

$$\text{Quantization Error} = \pm\frac{1}{2}LSB. \tag{40}$$

The quantization error of the Exacq ADC was found to be 1.22 mV per channel. Since the I and Q channels are combined to form the signal vector in the complex plane, the total worst case quantization error becomes 2.44 mV. This amount of quantization error can then be shown to produce worst case variations of ± 2 mV and $\pm 0.41^\circ$ in the magnitude and phase of the measured signal constellation points.

5.2.1 Posterior Object Placement

The first round of RAPM measurements involved placing the radio assay materials in the RAPM's posterior region. Materials were first placed in slot 1 and the signal constellation measurements were performed. The materials were then moved to slot 2 and the measurement process was repeated. The resulting signal constellations were then analyzed in Matlab with respect to the free space constellations to determine the changes of each constellation point's magnitude and phase. Note that in order to make the phase comparisons, all signal constellations with materials present were rotated until state 2 was aligned with state 2 of the free space constellation, as shown in Figure 53. This alignment was necessary in order to create a reference point between the free space constellation and the near-object constellations.

As seen from table 11, the effects of objects placed in the posterior region of a RAPM vary depending upon the material. Copper produced the greatest change in signal constellation point magnitude when placed in slot 1, with a 20 percent increase in the magnitude of state 2's constellation point, as shown in Figure 53. To explain how the constellation's magnitude can increase, we turn to antenna theory. Since the large conductor placed directly behind the RAPM serves as reflector for the

Table 11: Change in magnitude and phase of signal constellation points with respect to free space for different posterior object materials

Material	Distance from RAPM	State 0 ΔR(V),$\Delta\theta$	State 1 ΔR(V),$\Delta\theta$	State 2 ΔR(V),$\Delta\theta$	State 3 ΔR(V),$\Delta\theta$
Copper	0.17 λ	+0.04, +0.8°	+0.06, +4.2°	+0.03, 0.0°	+0.02, 0.1°
	0.58 λ	-0.01, -2.7°	-0.01, -3.8°	-0.01, 0.0°	-0.01, -2.6°
Aluminum	0.17 λ	0.00, -4.6°	+0.03, -10.3°	0.00, 0.0°	+0.02, 2.0°
	0.58 λ	0.00, -2.2°	-0.01, -4.8°	+0.01, 0.0°	0.00, -2.8°
Plywood (Pine)	0.93 λ	-0.01, -0.8°	0.00, -1.33°	-0.01, 0.0°	0.00, -0.1°
Plexiglass (Acrylic)	0.17 λ	0.00,-0.8°	-0.01,-3.1°	0.00,0.0°	0.00,-0.7°
	0.58 λ	0.00,+0.5°	-0.01,-0.5°	0.00,0.0°	0.00,+0.7°
Anti-Freeze	0.06 λ	0.00,-1.4°	0.00,-3.8°	0.00,0.0°	0.01,-0.5°
Steak	0.32 λ	-0.01,-1.3°	-0.01,-3.6°	-0.01,0.0°	0.00,-0.5°
Distilled Water	0.02 λ	-0.03,-3.8°	-0.02,-8.3°	-0.02,0.0°	0.00,-1.3°

patch's radiation, the effective gain of the antennas is increased, and the amount of backscattered power goes up, expanding the signal constellation . As the reflector is moved away from the RAPM and placed in slot two however, this gain increasing effect diminishes. For dielectric materials with high permittivity, such as distilled water, the opposite effect occurs. Attenuation of backscattered power occurs, shrinking the signal constellation. For distilled water, this effect was the most pronounced, with a worst case signal constellation point magnitude decrease of 13.2 percent with respect to free space, as shown in Figure 54.

The variations in constellation point phase, however, seem to have multiple dependencies. For example, copper produces positive phase shifts in slot 1 and negative phase shifts in slot 2, whereas aluminum produces negative phase shifts in both slots. This result is believed to be attributed to whether or not reflections from the conductor constructively or destructively interfere with the RAPM's main backscattered component. Furthermore, it is assumed that the phase of these reflections, and their resulting effect upon the phase of the RAPM's backscattered signal, is dependent upon the size and conductivity of the material.

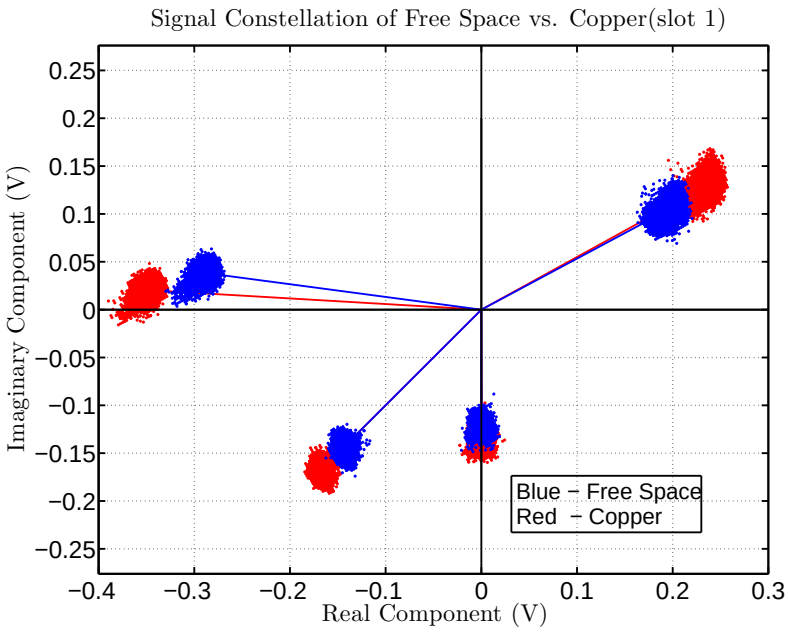

Figure 53: Backscatter signal constellation of copper(red) and free space(blue).

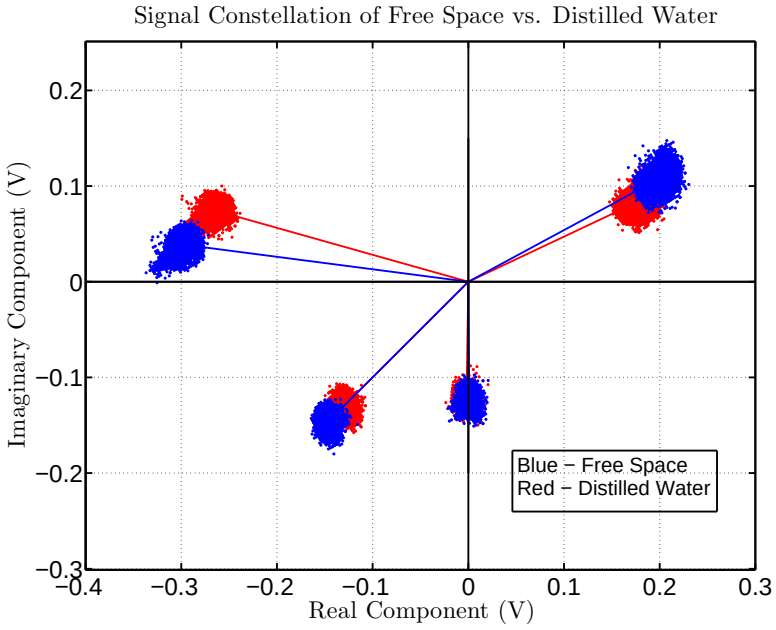

Figure 54: Backscatter signal constellation of distilled water(red) and free space(blue).

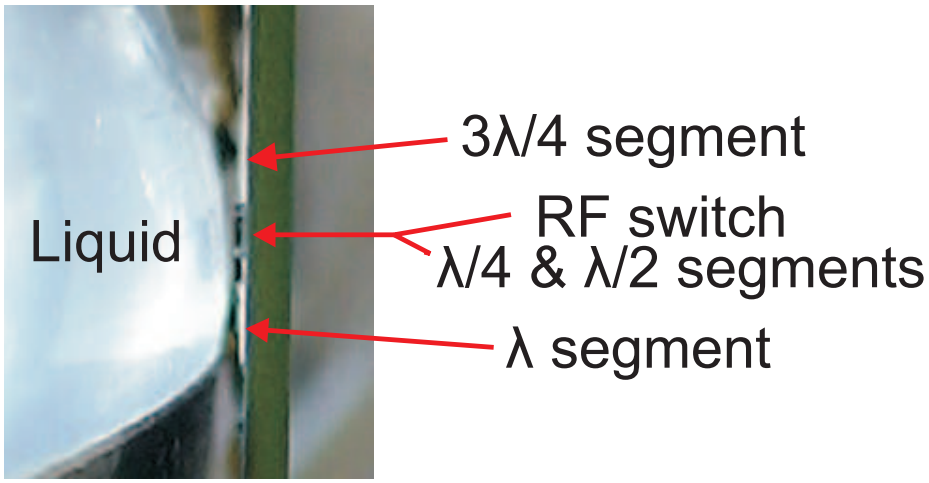

Figure 55: Close up of posterior liquid placement with respect to switching segment locations.

For dielectrics however, the phases of the signal constellation points are consistently retarded with respect to the free space measurements. This can be explained by looking at the RAPM-to-object separation distances in table 11. The anti-freeze, steak, and distilled water are electrically close to the circuit board, with separation distances of 0.06, 0.32 and 0.02 λ. Since the RAPM uses a CPWG transmission line topology, the propagation velocity of the backscatter signal is partially dependent upon the relative permittivity of the half space above the transmission line that is exposed to free space. Essentially, by bringing high permittivity materials close to the RAPM, the transmission lines of the switching network and antenna feeds are exposed to a medium with a permittivity greater than that of free space, thereby reducing the propagation velocity of signals through the switching network and antenna feeds. This reduction in propagation velocity then corresponds to with a backscatter signal phase retardation with respect to the homodyne receiver's local oscillator. For the RAPM, states 0 and 1 were found to have the greatest phase retardation, since the liquids placed in the posterior region were closest to the $\lambda/4$ and $\lambda/2$ switching segments, thereby creating the greatest change in half space relative permittivity, as shown in Figure 55. Note that the phase retardation produced by high permittivity

materials in the near posterior region of the RAPM could be resolved by designing a RAPM based upon a stripline transmission line topology.

5.2.2 Anterior Object Placement

5.2.2.1 Half Blockage

The RAPM was then characterized with materials placed in the channel between one of the RAPM patch antennas and the interrogator in order to determine how degradation of retrodirectivity affected the backscatter signal constellation. The materials were placed in the forwardmost slot of the antenna mount and were separated from the RAPM by distances of less than a wavelength. Due to the severe shrinking of the signal constellation caused by blockage losses, however, the phases of the signal constellation points could not be associated with their respective switching segments. As a result, only the average magnitudes of the signal constellations are compared to that of the free space constellation. These resulting changes in the magnitude of the backscatter signal constellation are listed in table 12.

As seen in the posterior measurements, the copper, due to its higher electrical conductivity, completely reflects the E-field component of the incident electromagnetic wave transmitted from the interrogator to one of the RAPM patches. This causes retrodirectivity to be lost and the RAPM gain to decrease, since incident signal energy must flow into the unblocked antenna, travel through the switching network, and out of the blocked antenna. The signal is then radiated out of the blocked antenna and reflected back into the antenna due to the nearby conductor. The backscatter signal then takes the reciprocal path back to the interrogator, doubling the RF FET losses, doubling the phase shift produced by each switching segment, and causing the RAPM radiation pattern to reduce to that of a single patch.

Significant signal constellation shrinkage also occurs when dielectrics with high permittivities block one of the RAPM's patches. Due to the lower intrinsic impedances associated with materials such as plywood, anti-freeze, steak, and distilled water,

Table 12: Change in magnitude of signal constellation points with respect to free space for different anterior object materials blocking half of the RAPM antenna array.

Material	Distance from RAPM	Average ΔR (V)	Shrinkage
Copper	0.63 λ	-0.17	-78.4 %
Aluminum	0.63 λ	-0.16	-74.6 %
Plywood (Pine)	0.87 λ	-0.06	-26.6 %
Anti-Freeze	0.05 λ	-0.12	-56.0 %
Steak	0.4λ	-0.14	-67.3 %
Distilled Water	0.01 λ	-0.15	-70.06%

impedance mismatches form between free space and the materials, causing reflection of energy incident from the interrogator. To support the concept that medium impedance mismatch is the reason for constellation shrinking, notice how constellation shrinking increases as relative permittivity increases from plywood to distilled water, respectively. This relative increase in relative permittivity can be correlated to decreasing material intrinsic impedance, which results in greater incident energy reflection and reduced RAPM backscattered power, since less power is transmitted through the medium and to the RAPM. To demonstrate the effects of conductors, low permittivity dielectrics, and high permittivity dielectrics on the RAPM backscatter signal constellation, Figures 56 through 58 have been provided.

5.2.2.2 Full Blockage

The radio assay materials were also placed to block both of channels between the RAPM's antennas and the interrogator and create a Rayleigh channel. As seen in the half blockage case, conductive materials introduced between the RAPM antennas and the interrogator severely attenuate the amount of power that reaches the RAPM, causing the backscatter signal constellation to collapse, as shown in Figure 59. For the dielectric materials, such as plexiglass, minimal constellation shrinkage occurred. This result was due to plexiglass' near free space permittivity of 2.6, which allowed for the majority of the incident energy to be transmitted through the plexiglass. Due

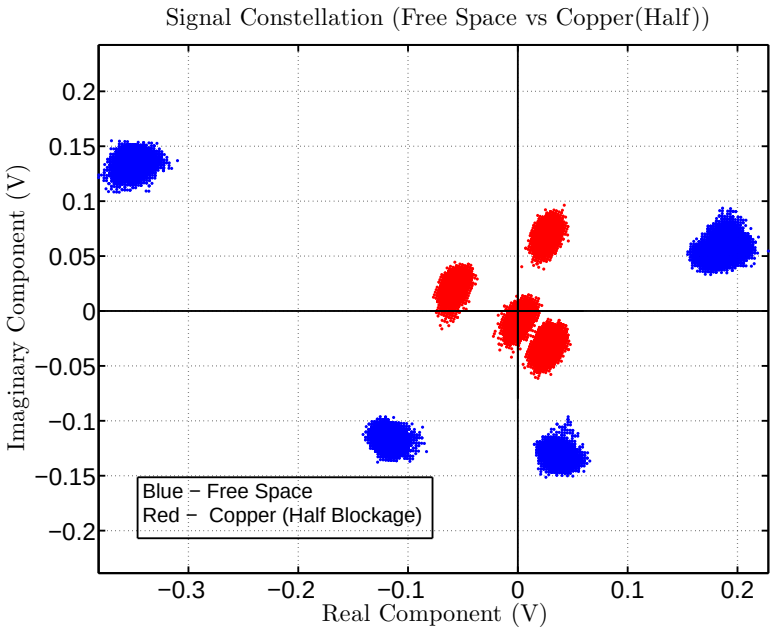

Figure 56: Backscatter signal constellation for RAPM with one antenna blocked by copper(red) vs free space(blue).

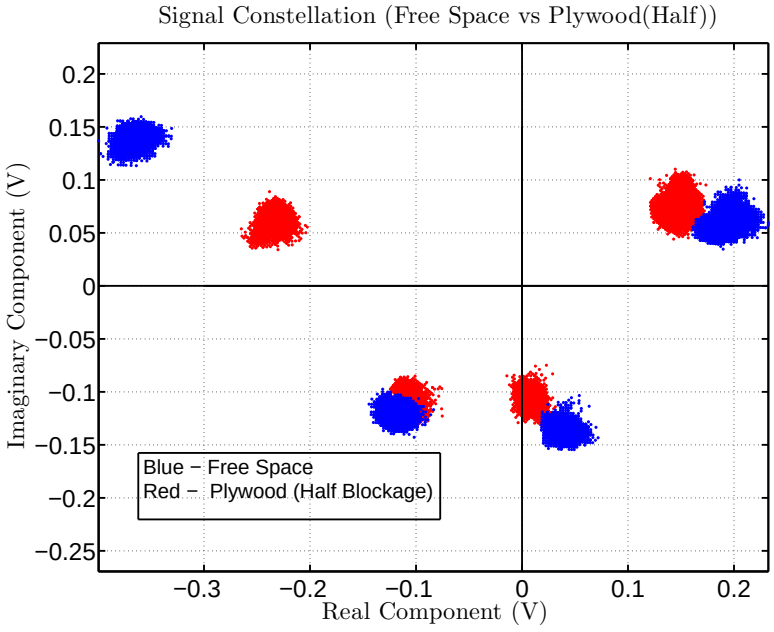

Figure 57: Backscatter signal constellation for RAPM with one antenna blocked by plywood(red) vs free space(blue).

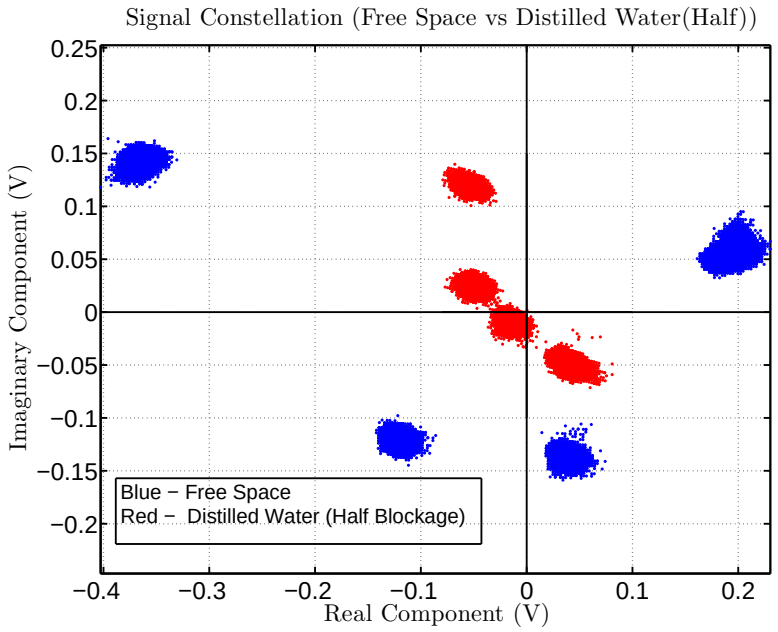

Figure 58: Backscatter signal constellation of for RAPM with one antenna blocked by distilled water(red) vs free space(blue).

Table 13: Change in magnitude of signal constellation points with respect to free space for different anterior object materials blocking both RAPM antennas.

Material	Distance from RAPM	*Average*ΔR (V)	Shrinkage
Copper	0.63 λ	-0.22	-95.6 %
Aluminum	0.63 λ	-0.21	-94.4 %
Plexiglass	0.63 λ	-0.02	-08.4 %

to the thickness of the plexiglass and its permittivity of 2.6, a slight reduction in the propagation speed of the backscatter signal occurred, inducing a constellation rotation of 68 degrees. For dielectrics with increasing permittivities, increased shrinking and rotation of the constellation would be expected due to medium impedance mismatches and reductions in propagation velocities. Figures 59 and 60 are provided to depict the effects of copper and plexiglass blockages, and table 13 is provided to demonstrate the amount of signal constellation shrinkage with respect to free space.

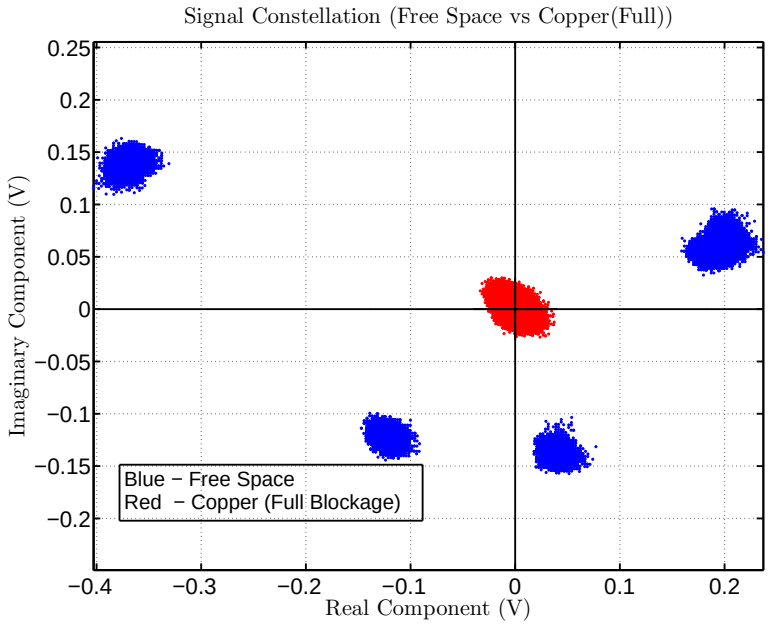

Figure 59: Backscatter signal constellation for RAPM with both antennas blocked by copper(red) vs free space(blue).

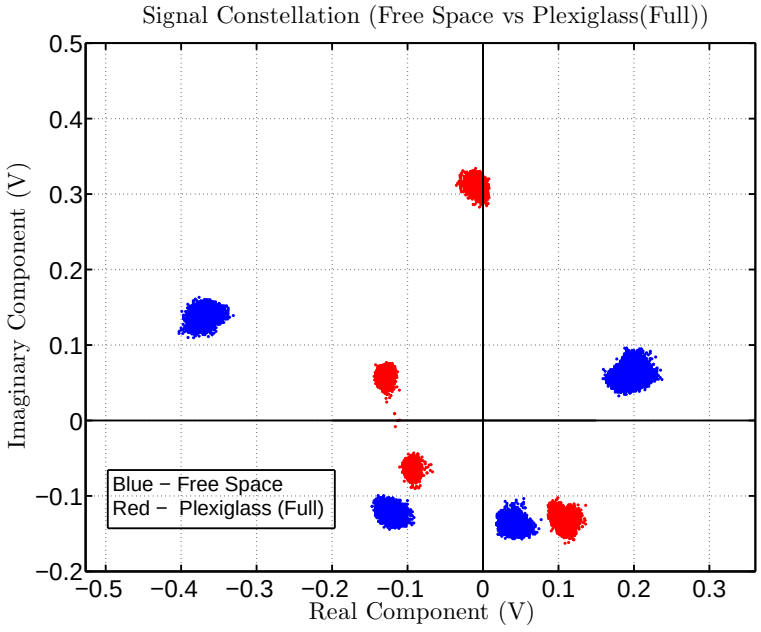

Figure 60: Backscatter signal constellation of for RAPM with both antennas blocked by plexiglass(red) vs free space(blue).

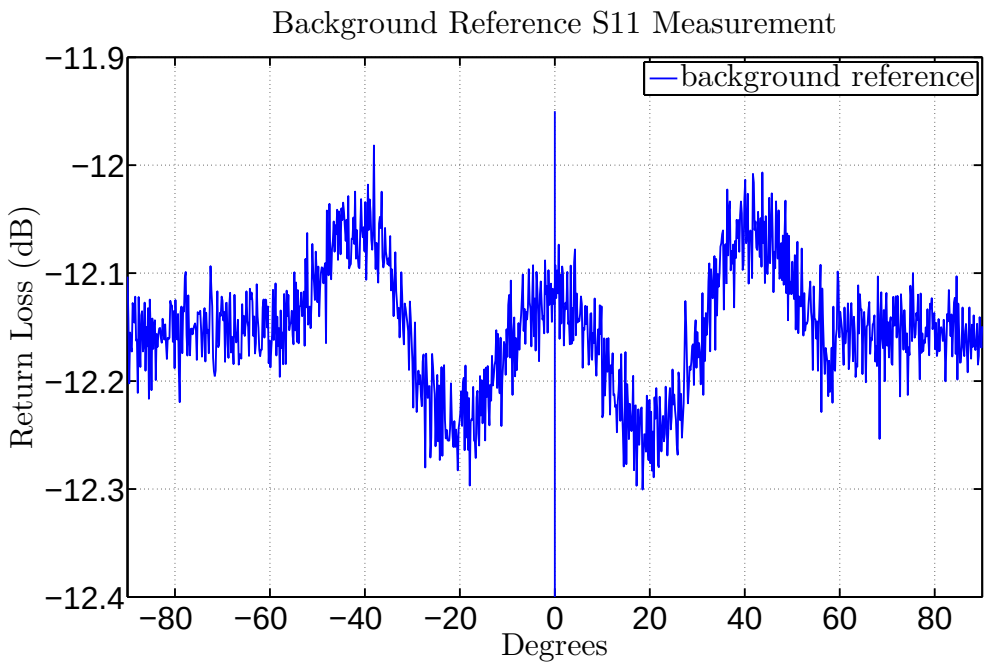

Figure 61: Return loss reference measurement for background subtraction.

5.3 Radar Cross Section

5.3.1 VNA Based Measurement Results

To characterize the increased beamwidth associated with using retrodirective arrays, the RCS was measured for a RAPM in free space. Using the single-port RCS measurement technique, the RCS was solved from the S11 measurement as:

$$\sigma = |S_{11}|^2 \frac{(4\pi)^3 r^4}{G_{horn}^2 \lambda^2}, \tag{41}$$

where $S11$ was recorded in the linear scale, G_{horn} represents the gain of the reference horn antenna connected to port 1 of the VNA, r is the separation distance between the horn excitation and the RAPM antenna array centroid, and λ is the free space wavelength. The background measurement, shown in Figure 61, was taken as the empty antenna mount was rotated from -90 to +90 degrees. This reference measurement was then subtracted from all other RCS measurements.

The RAPM was then placed in the antenna mount and RCS measurements were

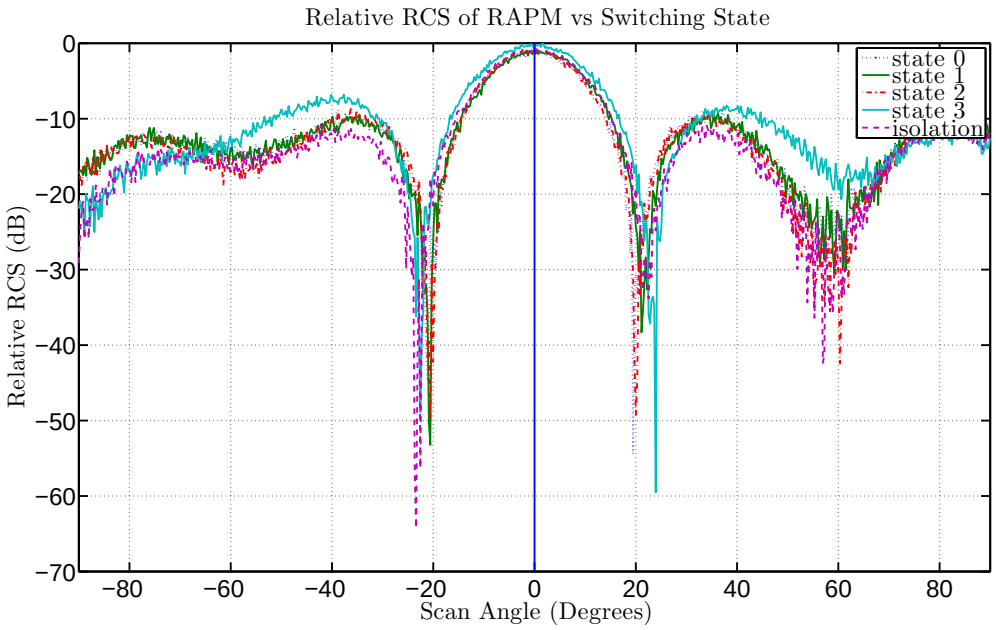

Figure 62: Comparison of RCS between all RAPM switching states and isolation.

taken with each switching segment connected. In an attempt to the compare the antenna mode and structural mode, an RCS measurement was also taken with the RAPM switches programmed to be in isolation. In doing so, both patch antenna feeds were terminated in open circuits, thereby eliminating the antenna mode of the RAPM. The relative RCS for these five cases is shown in Figure 62, and the scalar RCS of the RAPM was found to be approximately equal, regardless of which switching segment was connected to the antenna feeds.

The interesting RCS value in Figure 62 though, is the isolation measurement. In theory, the RCS should decrease when the antenna mode component is removed from the RCS of the RAPM, but it remains approximately equal to the cases where the antennas are connected through the switching network. The reason for this stems from the fact that patch antennas are inherently non-minimal scattering antennas, and that due to the large ground plane behind the antennas, the structural RCS component dominates the antenna mode RCS component.

5.3.2 Homodyne Receiver Based Measurement Results

In order to characterize the antenna mode RCS of the RAPM, the structural component needed to be removed. The signal constellation setup was used in place of the VNA setup, since it was capable of filtering out the structural component. By programming the RAPM to transmit a QPSK signal at a symbol rate of 1 MHz, modulated backscatter passed through the DC blocks of the homodyne receiver while the structural backscattered components of the patch and environmental scatters were filtered out, thereby allowing measurement of the RAPM's antenna mode.

To equate the VNA measurements with the homodyne receiver measurements, the magnitudes of the I and Q channels at the output of the homodyne receiver were summed and squared to achieve an equivalent received power, given as,

$$\text{Equivalent Total Channel Power} = \left(|I| + |Q|\right)^2, \tag{42}$$

where I and Q are the baseband voltages sampled at the output of the homodyne receiver. Note that to obtain an absolute RCS value, the system gain from the receive antenna to the ADC needs to be characterized. By dividing by the system gain, the power at the receive antenna can then be determined, and this value can be compared to the transmit power in order to determine the effective S11 at the interrogator antennas. For the sake of comparing beamwidths, however, the system gain was not characterized, and the raw equivalent power measured at the I and Q outputs of the receiver was used. By normalizing this equivalent power, the output of the homodyne receiver generated by the RAPM was then compared directly to the RCS measurements from the VNA setup.

The resulting RCS beamwidth comparisons between the VNA based measurement of the RAPM, the homodyne receiver based measurement of the RAPM, and the RCS of a copper sheet with dimensions equal to the RAPM are shown in Figure 63. The RCS beamwidth from the VNA measurement is approximately 10 degrees,

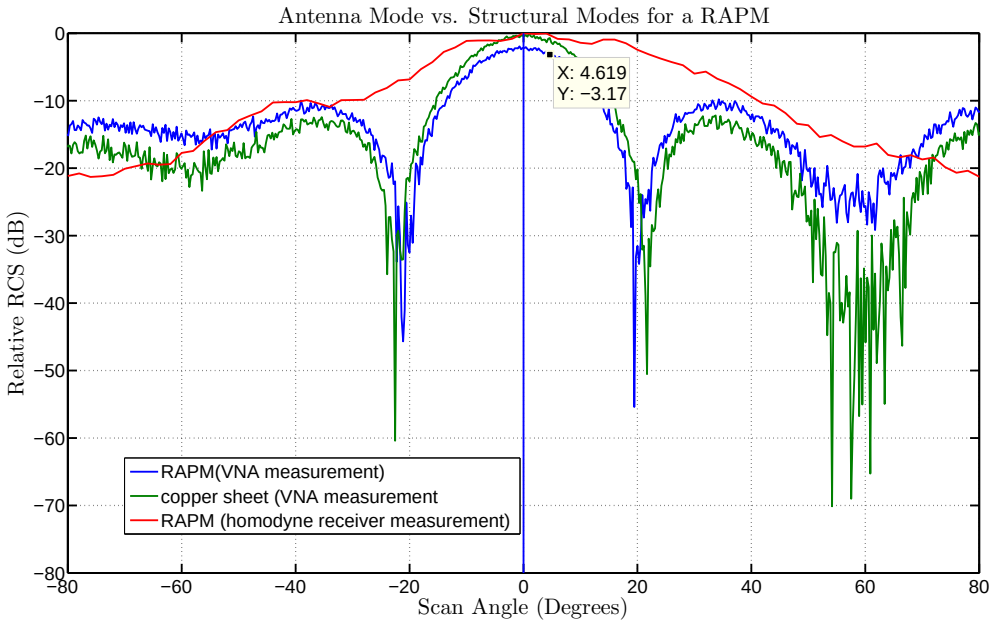

Figure 63: RCS beamwidth comparison between VNA and homodyne receiver measurement techniques.

whereas the RCS beamwidth from the homodyne receiver beamwidth is 37 degrees, clearly demonstrating that standard RCS measurement techniques are not capable of measuring the antenna mode RCS component of antennas with a large structural component. Furthermore, the RCS of the copper sheet was found to approximately equal to that of the VNA based RAPM measurement, confirming the theory that the structural component of the RAPM's ground plane dominated its overall RCS. To validate the homodyne receiver measurement, RCS beamwidth was then converted to antenna gain beamwidth and was found to be 74 degrees. This closely approximates the HFSS simulation result of 72 degrees for a single patch element.

CHAPTER VI

CONCLUSIONS

A prototyped RAPM QPSK backscatter modulator was designed after a theoretical analysis of its retrodirective properties and dyadic backscatter channel properties. A cablized SMA connector based version of the RAPM was characterized using a VNA to clearly define the phase shifting properties of the $\lambda/4$, $\lambda/2$, $3\lambda/4$, and λ switching segments. After the switching network failed to demonstrate the desired 90 degree phase difference between switching segments, a thorough analysis was performed by implementing microwave theory and Matlab simulations to determine the source of phase error. The error was confirmed through simulation to be a result of reflections generated between the RF switches and switching segments.

The RAPM's patch antennas were fully characterized and compared to the simulated values of HFSS. The relative permittivity of the FR-4 substrate was found to vary by ± 0.25. As a result, the FR-4 substrate needs to be fully characterized before doing antenna design in order to use the correct permittivity values in the patch design equations and antenna optimizations. The final patch antenna was found to have a resonant frequency of 5.73 GHz and a peak gain of approximately 4.2 dBi.

The final RAPM prototype was characterized for power consumption versus raw bitrate, bits per symbol, and the number of processing instructions per active cycle. For all bitrates, increasing the number of bits per symbol was found to decrease the power consumption of the RAPM due to a reduced transmission time per active cycle, which allowed the microcontroller to remain in a low power mode more often. The amount of power savings by increasing the number of bits per symbol was also found to become more significant as raw bitrates were increased and processing time per

active cycle was decreased.

For the backscatter signal constellation measurements, constellation warping was found to decrease as posterior conductors and high permittivity materials were moved away from the RAPM. The most significant constellation warping was produced by copper sheet and distilled water when placed less than a half wavelength from the RAPM. The greatest effect produced by the materials was constellation shrinking, with the copper producing reductions in constellation point magnitudes of up to 20 percent. For anterior measurements with one RAPM antenna blocked, significant constellation shrinkage of up to 78 percent and 70 percent were measured when copper sheet and distilled water were placed less than a wavelength in front of the RAPM. For Rayleigh channels where conductors were placed to fully block the channel between the RAPM and the interrogator, the signal constellation was found to completely collapse, with constellation shrinkage of 95.6 percent for copper sheet. Dielectric materials such as plexiglass however, with properties close to free space, produced minimal constellation shrinkage of 8.4 percent but significant constellation rotation of 68 degrees.

The RCS of the RAPM was found to be primarily driven by the structural scattering produced by the patch antennas' ground plane. As a result, the single-port VNA based measurement was unable to measure the antenna mode RCS of the RAPM's retrodirective array. A novel RCS measurement technique was implemented using a homodyne receiver to filter out the structural scattering component and measure only the antenna mode component. The relative antenna mode RCS beamwidth of the RAPM was then found to be 37 degrees, which was 27 degrees wider than the beamwidth of the structural scattering component measured through the single-port VNA technique.

6.1 Future Work

To expand the communication ability of the RAPM, the future design will be morphed into a retrodirective array quadrature modulator, or RAQM. The design change necessary is minimal and only requires placing a resistor between the switching segment and ground. In doing so, a power divider is created and the amount of power transmitted through a switching segment can be arbitrarily controlled to vary the amplitude of the backscattered signal.

Another interesting topic of study is the performance of a RAPM, or RAQM, under small signal fading conditions. Measurements of the fading distribution under different conditions would provide critical insight into how retrodirectivity affects a backscatter tag's performance. Theoretically, the increased number of diversity branches and increased beamwidth with respect to a single patch would result in increased performance of the RAPM under small signal fading conditions.

REFERENCES

[1] R. Langwieser, G. Lasser, C. Angerer, M. Fischer, and A. L. Scholtz, "Active carrier compensation for a multi-antenna rfid reader frontend," in *Microwave Symposium Digest*, May 2010, pp. 1532–1535.

[2] M. Kara, "Formulas for the computation of the physical properties of rectangular microstrip antennas elements with various substrate thicknesses," *Microwave and Opt. Technol. Lett.*, vol. 12, pp. 234–239, July 1996.

[3] D. M. Dobkin, *The RF in RFID: Passive UHF RFID in Practice.* Burlington, Massachusetts: Elsevier, 2008.

[4] J. D. Griffin, "High-frequency modulated backscatter communication using multiple antennas," Electrical and Computer Engineering Department, Georgia Institute of Technology, Atlanta, GA, Tech. Rep. PG-TR-090112-JDG, Jan. 2009.

[5] L. W. Mayer, R. Langweiser, and A. L. Scholtz, "Evaluation of passive carrier-suppression techniques for uhf rifd systems," in *Proc. of IEEE MTT-S International Microwave Workshop on Wireless Sensing, Local Positioning, and RFID*, Sept. 2009, p. 1.

[6] *EPC^{TM}Radio-Frequency Identity Protocols Class-1 Generation-2 UHF RFID Protocol for Communications at 860 MHz - 960 MHz*, EPCglocal Inc. Std., Rev. 1.0.9, Jan. 2008. [Online]. Available: www.gs1.org

[7] I. Zalbide, J. Vicario, and I. Vélez, "Power and energy optimization of the digital core of a gen2 long range full passive rfid sensor tag," in *Proc. of IEEE Intl. Conf. on RFID*, Apr. 2008, pp. 126–133.

[8] P. V. Nikitin and K. Rao, "Theory and measurement of backscattering from rfid tags," *IEEE Antennas and Propagation Magazine*, vol. 48, no. 6, pp. 212–218, Dec. 2006.

[9] J. F. Dickson, "On-chip high-voltage generation in mnos integrated circuits using an improved voltage multiplier technique," *IEEE Journal of Solid-State Circuits*, vol. SC-11, no. 3, pp. 374–378, June 1976.

[10] S. Thomas and M. S. Reynolds, "Qam backscatter for passive uhf rfid tags," in *Proc. of IEEE RFID*, Apr. 2010, pp. 210–214.

[11] *Code of Federal Regulations, Title 47, Part 15*, Federal Communications Commission Std., Dec. 2010.

[12] D. Dardari, R. D'Errico, C. Roblin, A. Sibille, and M. Z. Win, "Ultrawide bandwith rfid: The next generation?" in *Proc. of the IEEE*, vol. 98, no. 9, Sept. 2010, pp. 1570–1582.

[13] H. T. Friis, "A note on a simple transmission formula," in *Proc. of the I.R.E and Waves and Electrons*, May 1946, pp. 254–256.

[14] J. D. Griffin and G. D. Durgin, "Complete link budgets for backscatter-radio and rfid systems," *IEEE Antennas and Propagation Magazine*, vol. 51, no. 2, pp. 11–25, Apr. 2009.

[15] J. D. Griffin, G. D. Durgin, A. Haldi, and B. Kippelen, "Rf tag antenna performance on various materials using radio link budgets," *IEEE Antennas and Wireless Propagation Letters*, vol. 5, pp. 247–250, Dec. 2006.

[16] L. C. Van Atta, "Electromagnetic reflector," US Patent 2,908,002, Oct., 1959.

[17] J. R. Smith, A. P. Sample, P. S. Powledge, S. Roy, and A. Mamishev, "A wirelessly-powered platform for sensing and computation," in *Proc. of UBICOMP 2006: Ubiquitous Computing*, vol. 4206, 2006, pp. 495–506.

[18] S.-J. Chung, S.-M. Chen, and Y.-C. Lee, "A novel bi-directional amplifier with applications in active van atta retrodirective arrays," *IEEE Transactions on microwave theory and techniques*, vol. 51, pp. 542–547, Feb. 2003.

[19] C. Y. Pon, "Retrodirective array using the heterodyne technique," *IEEE Transactions on Antennas and Propagation*, vol. 12, pp. 176–180, Mar. 1964.

[20] S. Lim, K. Leong, and T. Itoh, "Adaptive power controllable retrodirective array system for wireless sensor server applications," *IEEE Transactions on Mircowave Theory and Techniques*, vol. 53, pp. 3735–3743, Dec. 2005.

[21] G. M. Coutts, R. R. Mansour, and S. K. Chaudhuri, "A frequency steerable multi-mode parasitic patch array for passive rfid applications," in *Microwave Symposium Digest*, June 2006, pp. 186–189.

[22] G. D. Durgin, *Space-Time Wireless Channels*. Upper Saddle River, NJ: Prentice Hall Ptr, 2003.

[23] J. D. Griffin and G. D. Durgin, "Gains for rf tags using multiple antennas," *IEEE Transactions on Antennas and Propagation*, vol. 56, pp. 563–570, Feb. 2008.

[24] C. A. Balanis, *Antenna Theory: Analysis and Design*. New York, NY: John Wiley & Sons, Inc., 1997.

[25] M. J. Gay and R. Pangier, "Making sense of laminate dielectric properties," Isola Group, Tech. Rep., 2008.

[26] *Specification for Base Materials for Rigid and Multilayer Printed Boards*, IPC Std., Aug. 2009. [Online]. Available: www.ipc.org

[27] R. Garg, P. Bhartia, I. Bahl, and A. Ittipiboon, *Microstrip Antenna Design Handbook*. Norwood, MA: Artech House, 2001.

[28] P. Liang, "The development and application of low dk material," in *Proc. of Microsystems, Packaging, Assembly and Circuits Technology*, Oct. 2007, pp. 363–368.

[29] A. R. Djordjević, R. M. Biljić, V. D. Likar-Smiljanić, and T. K. Sarkar, "Wideband frequency-domain characterization of fr-4 and time-domain causality," *IEEE Transactions on Electromagntic Compatibiity*, vol. 43, pp. 662–667, Aug. 2001.

[30] J. D. Griffin, "A radio assay for the study of radio frequency tag antenna performance," Electrical and Computer Engineering Department, Georgia Institute of Technology, Atlanta, GA, Tech. Rep. PG-TR-050504-JDG, May 2005.